The Galaxy Zoo survey for giant AGN-ionized clouds: past and present black-hole accretion events

William C. Keel[1,2,3][*], S. Drew Chojnowski[2,3,4], Vardha N. Bennert[5], 6,
Kevin Schawinski[7,8,9], Chris J. Lintott[10,11], Stuart Lynn[2,10], Anna Pancoast[5],
Chelsea Harris[5], A.M. Nierenberg[5], Alessandro Sonnenfeld[5], & Richard Proctor[12]

[1] *Department of Physics and Astronomy, University of Alabama, Box 870324, Tuscaloosa, AL 35487, USA*
[2] *Visiting Astronomer, Kitt Peak National Observatory, operated by AURA, Inc. under contract to the US National*
Science Foundation.
[3] *SARA Observatory*
[4] *Texas Christian University, Forth Worth, TX 76129 USA*
[5] *Department of Physics, University of California, Santa Barbara, CA 93106 USA*
[6] *Physics Department, California Polytechnic State University, San Luis Obispo, CA 93407, USA* [7] *Department of Physics, Yale University, New Haven*
[8] *Yale Center for Astronomy and Astrophysics, Yale University, P.O.Box 208121, New Haven, CT 06520, USA*
[9] *Einstein Fellow*
[10] *Astrophysics, Oxford University*
[11] *Adler Planetarium, 1300 S. Lakeshore Drive, Chicago, IL 60605*
[12] *Waveney Consulting, Wimborne, Dorset BH21 3QY*

ABSTRACT
Some active galactic nuclei (AGN) are surrounded by extended emission-line regions (EELRs), which trace both the illumination pattern of escaping radiation and its history over the light-travel time from the AGN to the gas. From a new set of such EELRs, we present evidence that the AGN in many Seyfert galaxies undergo luminous episodes 0.2–2×10^5 years in duration. Motivated by the discovery of the spectacular nebula known as Hanny's Voorwerp, ionized by a powerful AGN which has apparently faded dramatically within $\approx 10^5$ years, Galaxy Zoo volunteers have carried out both targeted and serendipitous searches for similar emission-line clouds around low-redshift galaxies. We present the resulting list of candidates and describe spectroscopy identifying 19 galaxies with AGN-ionized regions at projected radii $r_{proj} > 10$ kpc. This search recovered known EELRs (such as Mkn 78, Mkn 266, and NGC 5252) and identified additional previously unknown cases, one with detected emission to $r = 37$ kpc. One new Sy 2 was identified. At least 14/19 are in interacting or merging systems, suggesting that tidal tails are a prime source of distant gas out of the galaxy plane to be ionized by an AGN. We see a mix of one- and two-sided structures, with observed cone angles from 23–112°. We consider the energy balance in the ionized clouds, with lower and upper bounds on ionizing luminosity from recombination and ionization-parameter arguments, and estimate the luminosity of the core from the far-infrared data. The implied ratio of ionizing radiation seen by the clouds to that emitted by the nucleus, on the assumption of a nonvariable nuclear source, ranges from 0.02 to > 12; 7/19 exceed unity. Small values fit well with a heavily obscured AGN in which only a small fraction of the ionizing output escapes to be traced by surrounding gas. However, large values may require that the AGN has faded over tens of thousands of years, giving us several examples of systems in which such dramatic long-period variation has occurred; this is the only current technique for addressing these timescales in AGN history. The relative numbers of faded and non-faded objects we infer, and the projected extents of the ionized regions, give our estimate (0.2–2×10^5 years) for the length of individual bright phases.

Key words: galaxies: Seyfert — galaxies: ISM — galaxies: active

[*] E-mail: wkeel@ua.edu

1   INTRODUCTION

The compact sizes of the central engines of active galactic nuclei (AGN) have long driven study of their distant surroundings for clues to their geometry and interaction with the surrounding galaxy. Observations of gas seen many kpc from the AGN itself have proven fruitful in offering views of the core from different angles, and implicitly at different times.

Narrowband images revealed extended emission-line regions (EELRs) around some luminous AGN, particularly radio-loud QSOs as well as radio galaxies, as reviewed by Stockton, Fu, & Canalizo (2006). Similar structures in lower-luminosity Seyfert galaxies often appear as single or double triangles in projection (Unger et al. 1987, Tadhunter & Tsvetanov 1989), generally interpreted as ionization cones. When small-scale radio jets are present, they lie within the ionization cones. However, in many cases, the gas must be ionized by radiation from the nucleus rather than direct interaction with a jet or outflow, as seen from narrow linewidths and (particularly diagnostic) modest electron temperatures, both of which would be much larger in the presence of shocks fast enough to match the observed ionization levels. This is particularly true for very large EELRs, where interaction with the radio jet or an origin in outflows alone become less and less likely. In fact, the best-defined ionization cones are seen in radio-quiet objects (Wilson 1996).

This is one line of evidence linking large-scale structures to the small-scale obscuring regions ("tori") implied by other arguments for a unification scheme (Antonucci 1993), in which Seyferts of types 1 and 2 are part of a single parent population, appearing different based on how our line of sight passes this torus. The emission-line structures can be large and well-resolved, offering a way to measure the opening angle over which ionizing radiation escapes. Some previous studies have also noted that these emission-line clouds provide a view to the immediate past of the AGN, via light-travel time to the cloud and then toward us (Dadina et al. 2010).

Using extended emission-line clouds as probes of AGN history came of age with the discovery of Hanny's Voorwerp, a high-ionization region extending 45 kpc in projection from the LINER IC 2497 at $z = 0.05$ (Lintott et al. 2009). Linewidths and electron temperature indicate that the gas is photoionized rather than shock-excited, while a combination of ionization-parameter and recombination arguments bound the required nuclear ionizing luminosity to be $1 - 4 \times 10^{45}$ erg s^{-1}. However, X-ray spectroscopy shows the nucleus of IC 2497 to be only modestly absorbed, with ionizing luminosity only $\approx 10^{42}$ erg s^{-1} (Schawinski et al. 2010a). It is difficult to avoid the conclusion that the nucleus of IC 2497 was in fact a QSO (the nearest known luminous QSO) until roughly 10^5 years before our current view, and has faded dramatically in the interim; radio and HST observations offer hints that some of its energy output may have switched to kinetic forms over this timespan (Josza et al. 2009, Rampadarath et al. 2010, Schawinski et al. 2010a, Keel et al. 2011). The unlikeliness of the nearest QSO showing highly unusual behaviour suggests that such variations may be common among AGN, prompting us to re-examine the incidence and properties of extended ionized clouds around nearby AGN. Such an examination should not be confined to

catalogued AGN, since the most interesting objects - those which have faded dramatically - may no longer appear as spectroscopically classified AGN.

Hanny's Voorwerp was first noted by Dutch teacher Hanny van Arkel in the course of the Galaxy Zoo project (Lintott et al. 2008), on the basis of its unusual structure and colour. In view of the interest of similar ionized clouds for study of both the history and obscuration of AGN, participants in the Galaxy Zoo project have carried out a wide search for such clouds using data from the Sloan Digital Sky Survey (SDSS). They examined both known AGN hosts and galaxies not known to have AGN, using the distinctive colour of highly-ionized regions across the SDSS *gri* filters as a first selection criterion. We present the results of further analysis of the SDSS images, narrow-band imaging, and spectroscopy, yielding a list of 19 galaxies with AGN-photoionized clouds detected to beyond 10 kpc from the nuclei (many of which are newly identified). We consider constraints on changes in ionizing luminosity for these, and identify several as the most likely candidates for the kind of long-term fading seen in IC 2497 and Hanny's Voorwerp.

2   SEARCHES FOR EMISSION-LINE CLOUDS

The Galaxy Zoo search for giant AGN-ionized clouds combined both targeted and serendipitous approaches, to combine a complete examination of known AGN hosts with the possibility of finding ionized clouds around AGN which are yet unknown or in fact optically unseen. In the targeted search, we formed a sample of potential AGN at $z < 0.1$. This combined all galaxies whose SDSS pipeline emission-line ratios put them in either the AGN or composite regions of the Baldwin-Phillips-Terlevich (BPT) diagram (Baldwin, Phillips, & Terlevich 1981, as revised by Kewley et al. 2001 and Kauffmann et al. 2003) using [O III]/Hβ and [N II]/Hα, and all additional objects listed in the Veron-Cetty & Veron catalog (Veron-Cetty & Veron 2010) at $z < 0.1$ falling within the SDSS data release 7 (DR7) area. This addition accounted for AGN with no SDSS nuclear spectrum, either because they are relatively bright or, more often, because fibre collisions or sampling rules prevented their selection for spectra, and type 1 AGN where the pipeline spectroscopic classification is less reliable than for narrow-line objects. The merged AGN sample, designed to err on the side of inclusion in borderline cases, included 18,116 objects. With a web interface designed by RP, 199 participants examined all of these within a 6-week period in 2009, marking each as certain, possible, or lacking an extended emission region. These emission regions have distinctive signatures in both morphology and colour from the SDSS data. They do not follow the usual spiral or annular distributions of star formation in disc galaxies. Such regions show unusual colours in the SDSS composite images, which map *gri* bands to blue, green, and red (Lupton et al. 2004). Hence strong [O III] at low redshift is rendered as a pure blue, as in the discovery of Hanny's Voorwerp. A combination of strong [O III] and significant Hα+[N II] appears purple; beyond about $z = 0.1$, [O III] falls in the gap between g and r filters, so our search technique loses utility until [O III] is well within the r band, when the galaxies have much smaller angular sizes. This

subproject was known as the "voorwerpje hunt", using the Dutch diminutive form of Voorwerp.

Each galaxy was examined by at least ten participants; 199 Zoo volunteers participated in this program, seven of whom examined the entire sample. The final average number of votes was 11.2 per object. After this screening process, a straightforward ranking was by relative numbers of "yes" (weight=1), "maybe" (weight=0.5), and "no" (weighted zero) votes.

The most interesting results of such a search would be galaxies with prominent AGN-ionized clouds in which we don't see the AGN, either because of strong obscuration or dramatic variability during the light-travel time from the nucleus to the clouds. These would not be found by targeting known AGN, and neither would clouds around AGN which do not have catalogued spectral information. Accordingly, we also posted a request on the Galaxy Zoo discussion forum, with examples of confirmed AGN clouds and various kinds of similar-appearing image artifacts. Participants were invited to post possible cases from among the galaxies they saw in the ordinary course of the Galaxy Zoo classification programs (Lintott et al. 2008), and some active users reposted examples from other discussion threads. The resulting followups[1] provided an additional sample for investigation; WCK also checked all the threads with image discussion for more such objects, early examples of which instigated this search on the first place. To reduce the number of false positives caused by extended star-forming regions or starburst winds, objects were removed from consideration if an SDSS spectrum shows emission lines characteristic of a starburst. Remaining candidates were examined first on the SDSS composite images for appropriate colour and geometry, and the most promising ones were carried forward for further analysis.

Both targeted and serendipitous lists overlap for many objects with bright emission-line structures, and recover such well-studied cases from the literature as Mkn 266, NGC 5252 and Mkn 78; we observed these so as to have a consistent set of spectra for comparison. The entire list of candidates is given in Table 8. In the Survey column, S or T denotes whether the object was found in the serendipitous survey, the targeted survey of known AGN, or both. The type of nuclear optical spectrum is listed as Sy 1/1.5/1.9/2, LINER, SB for starburst, or nonAGN for an ordinary stellar population. The final column indicates which Galaxy Zoo participant (by user name) first posted objects in the serendipitous survey.

2.1 SDSS image analysis and new images

For both subsamples, further winnowing had the same steps. Most importantly, we reanalyzed the SDSS images, to verify that the features do not have continuum counterparts, and eliminate artifacts caused by imperfect registration of the images when forming the colour composites. This effect is of particular concern for Seyfert 1 nuclei, where the PSF of the bright nucleus can produce a decentered colour signature if one of the constituent images is slightly misregistered; Sy 1
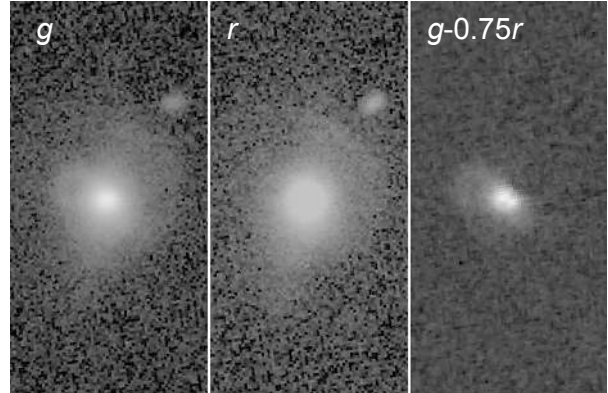

Figure 1. Linear combination of SDSS images to isolate candidate [O III] emission regions, shown with SDSS J143029.88+133912.0 (the Teacup AGN). The region shown spans 64×128 SDSS pixels, or 25.3×50.6", with north at the top. Each image is displayed with a logarithmic intensity mapping, with a small zero point offset to reduce the effects of noise around zero. At the redshift $z = 0.085$ of this galaxy, Hα and [N II] emission fall redward of the r filter band (response 0.2% of peak) so the r image is used as a continuum estimate.

galaxy image are more vulnerable to this artifact than normal galactic nuclei. Since many candidates (including some with spectroscopic confirmation) have "purple haze" on the SDSS images, which could either be genuinely extended and somewhat amorphous [O III] and Hα or an artifact, this was a helpful step. We adopted a tomographic approach, taking one of the SDSS bands free of strong emission lines (r or i, depending on redshift) as an estimate of the structure of starlight in the galaxy. This was scaled to match the largest part of the g structure, iteratively when necessary. This is illustrated in Fig. 1, isolating the emission-line loop in SDSS 1430+13 (nicknamed the Teacup AGN because of this structure). Chojnowski and Keel inspected the best subtraction among various scalings (often a compromise, due to colour gradients within the galaxy) to assess the reality of extended emission-line features not associated with clear spiral arms or stellar rings. These results let us rank the candidate lists from both targeted and serendipitous searches in order of significance of the emission-line structures based on the SDSS images themselves. We used these results to limit the number of candidates from the targeted search to the top 50; below this there were no convincing candidates based on more detailed analysis of the SDSS images.

Where appropriate filters were available for [O III] or Hα at a galaxy's redshift, some candidates were imaged at the remote SARA 1m (Kitt Peak) and 0.6m (Cerro Tololo) telescopes. For [O III], we used a filter centered at 5100 Å with half-transmission width 100Å , useable for the redshift range $z = 0.009 - 0.025$. At Hα, both telescopes have stepped sets of filters 75 Å apart with FWHM ~ 75 Å . Continuum was taken from V, R or g, r, appropriately scaled for subtraction to show net emission-line structures. These data are particularly helpful in tracing the emission-line structures of UGC 7342 (Fig. 2) and SDSS 2201+11 (Fig. 3).
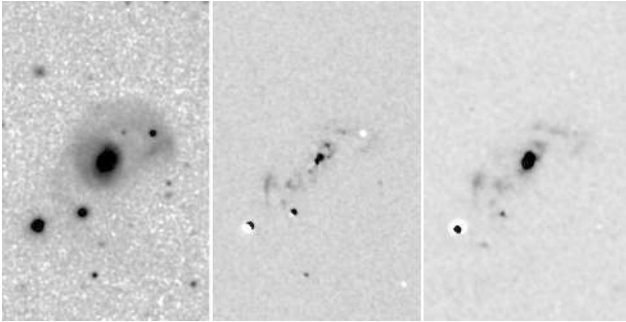
---

[1] in http://www.galaxyzooforum.org/index.php?topic=275014.0

Figure 2. The extended clouds in UGC 7342. Left, the starlight continuum in a band at 6450 Å from the SARA 1m telescope. Center, an estimated [O III] image from the SDSS data as in Fig. 1. Right, continuum-subtracted Hα image from the SARA 1m. North is at the top and east to the left; the field shown spans 97 × 150 arcseconds.
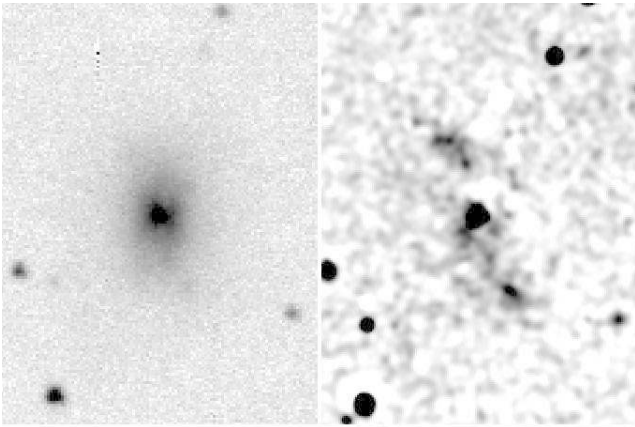

Figure 3. The extended clouds in SDSS 2201+11. Left, a *g* image from the SARA-S 0.6m telescope, showing the dusty disk. Right, continuum-subtracted [O III] image from the SARA-N 1m telescope, smoothed by a Gaussian of 2.0" FWHM. North is at the top and east to the left; the field shown spans 64 × 84 arcseconds.

2.2 Spectroscopy

To confirm that regions are in fact ionized by AGN, and derive diagnostic emission-line properties, we carried out long-slit spectroscopy for the highest-priority candidates. Observations used the GoldCam spectrograph at the 2.1m telescope of Kitt Peak National Observatory and the Kast double spectrograph at the 3m Shane telescope of Lick Observatory. Table 1 compares the setups used for each session. The slit width was set at 2" for all these observations, and the spectrographs were rotated to sample the most extended known structures of each galaxy. Scheduling allowed us to reduce the Kitt Peak data before the first Lick observing

run, so that the 3m spectra could be concentrated on the most interesting galaxies. Total exposures ranged from 30 minutes, for initial reconnaissance to see whether an object might host AGN clouds, to 2 hours for weaker lines in confirmed targets. Either night-sky line or interspersed lamp observations were used to track flexure, as needed. Reduction used the *longslit* package in IRAF[2] (Tody 1986), and included rebinning to a linear wavelength scale, sky subtraction, and flux calibration. Spectrophotometric standard stars were observed to set the flux scale; in a few cases where passing clouds were an issue, the spectra were scaled so that the nucleus within a 2 × 3" region matched the flux of the SDSS spectra.

Our identification of these extended regions as being photoionized by AGN rests on three results - location in the strong-line BPT diagram, strength of the high-ionization species He II and [Ne V], and electron temperature consistent with photoionization but not with shock ionization. We classify emission regions based on the "BPT" line-ratio diagrams pioneered for galactic nuclei by Baldwin, Phillips, & Terlevich (1981) and refined by Veilleux & Osterbrock (1987), with caution based on the possibility that some of the external gas could have much lower metal abundances than found in galactic nuclei (as seen in Hanny's Voorwerp; Lintott et al. 2009). Abundance effects in gas photoionized by AGN, as manifested in the BPT diagrams, have been considered in calculations by Bennert et al. (2006a). The largest effect is higher equilibrium temperature at lower O abundance, since it is an important coolant, which drives stronger forbidden lines and higher ionization levels until very low levels (0.1 solar) are reached. In any case, the abundance changes are not large enough to move these clouds across the empirical AGN/starburst ionization boundary. Furthermore, in the galaxies where we have data covering the red emission lines, the clouds' locations in the (essentially abundance-independent) auxiliary BPT diagram of [O III]/Hβ versus [O I]/Hα also indicated photoionization by an AGN continuum. The various BPT diagrams are compared for Points along the slit in each of the clouds we classify as AGN-ionized in Fig. 4. This classification is examined more closely in the context of its radial behavior in the next section.

Independent of these line ratios, strong He II λ4686 or [Ne V] λλ3346, 3426 indicate photoionization by a harder continuum than provided by young stars, and resolved emission from these species is immediately diagnostic of AGN photoionization in this context. For some objects, we do not have red data; in these, we classify the cloud as AGN-ionized based on the presence of the high-ionization lines or continuity of line ratios with the nucleus. Line ratios in the extreme blue may be affected in subtle ways by atmospheric dispersion (Filippenko 1982); the scheduling of our observations forced us to observe most targets at hour angles which did not allow us to put the slit simultaneously along the structures of interest and close to the parallactic angle. The extended regions we observe are generally wider than the
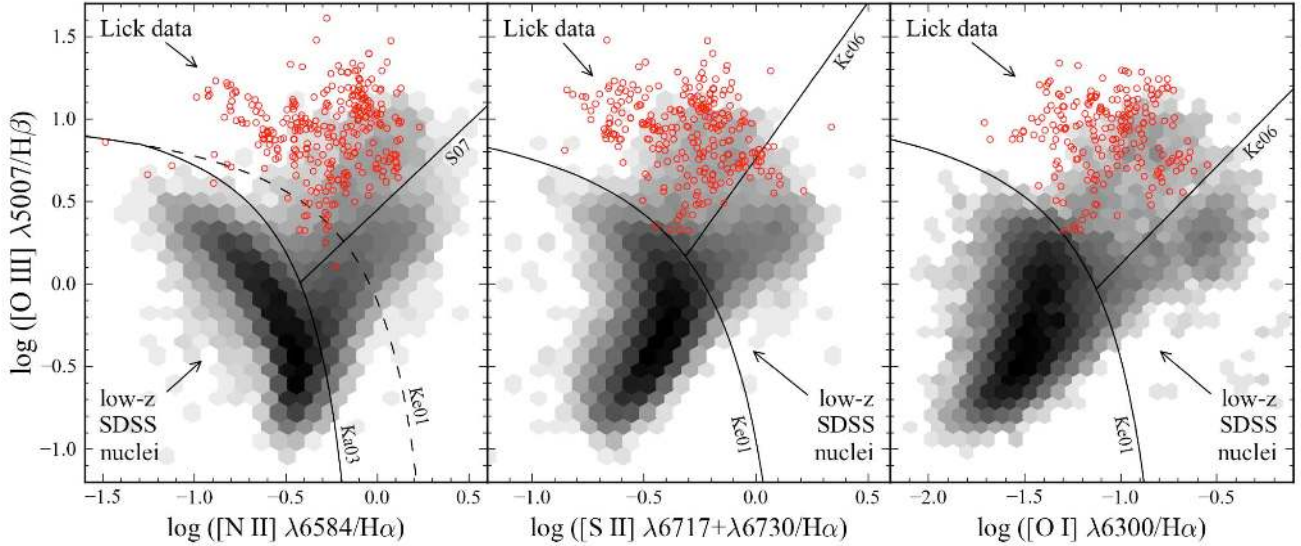
Figure 4. Summary Baldwin-Phillips-Terlevich (BPT) diagrams for the Lick spectra, where we measured the requisite red emission lines. Circles indicate points along the slit for extended clouds classified as AGN-ionized and the host nuclei. Gray-scale background shows the density of points from all low-redshift SDSS galactic nuclei, as in Schawinski et al. (2010b). The dividing lines between regions photoionized by AGN and by hot stars are shown as given by Kewley et al. (2001; Ke01) and by Kauffmann et al. (2003; Ka03).

slit; to first order line intensities are not affected by atmospheric refraction, since we calibrate with standard stars at low airmass. Some of the Lick blue spectra have atmospheric dispersion contributing as much as 3" of offset along the slit from red to blue ends of the spectrum, important only for the nuclei and corrected in extracting their spectra.

The BPT diagrams are designed to separate common sources of photoionization in galaxies; temperature and kinematic data are also important to understand whether shocks pay a significant role. In a few cases, the [O III] $\lambda4363$ line was measured in the extended clouds with sufficient signal-to-noise ratio for a measurement of the electron temperature via its ratio to the strong $\lambda\lambda4959, 5007$ lines. Using the IRAF task *temden*, which implements the algorithm of Shaw & Dufour (2007), and considering $n_e < 100$ cm^{-3}, we find T_e values of $18,600 \pm 1000$ in the SDSS 2201+11, $13,300 \pm 300$ for Mkn 266, and $15,400 \pm 500$ for the Teacup system. These confirm that the gas is photoionized rather than shocked; for comparison, temperatures in the [O III] zone of supernova

remnants (including some with lower ionization levels than in these clouds) range from 20,000-69,000 K (e.g., Fesen et al. 1982, Wallerstein & Balick 1990, Morse et al. 1995). In addition, very high shock velocities ≈ 400 km s^{-1} are needed to produce significant [Ne V] emission Dopita & Sutherland (1996). This is far in excess of the local velocity ranges we observe (section 6); even though we would not necessarily observe material on both sides of a shock in the same ion, it is difficult to envision a situation with large-scale shocks of this velocity without observable velocity widths or structures exceeding 100 k s^{-1}.

While not the main thrust of our survey, it is worth noting that we find a few instances of either double AGN in interacting systems, or AGN in the fainter member of a close pair (Mkn 177, Was 49, possibly SDSS J111100.60-005334.9 and SDSS J142522.28+141126.5). These may be worth deeper spectroscopy in the context of mapping AGN obscuration; if a high-ionization component can be isolated in the gas of the other galaxy, its distribution could show

where ionizing radiation escapes any circumnuclear absorbing structure. This offers a distinct way of tracing the ionizing radiation even in the absence of extensive gaseous tidal features, in an approach that has been discussed for Was 49ab by Moran et al. (1992).

Table 4 lists the results of our spectroscopy. Confirmed, resolved clouds ionized by the AGN are separated from other results (unresolved AGN emission, extended star-forming regions denoted as H II, and so on). The instruments used are denoted by GCam (Kitt Peak GoldCam) and Lick (Lick 3m with Kast spectrograph). New redshifts and spectral classifications are marked with asterisks. We separate the AGN clouds of most interest based on the detected extent of [O III] $\lambda5007$; our spectra have a lower detection threshold than our images for this, roughly 10^{-16} erg cm^{-2} s^{-1} arcsec^{-2} for emission regions a few arcseconds in size. Spectra of the nuclei and representative cloud regions are shown in Figs. 5 and 6. Table 5 lists emission-line ratios and selected fluxes for the same regions plotted in these figures. Fluxes are given both for [O III] $\lambda5007$ and Hα, since these were usually measure with different gratings and detectors. For some of the nuclei, correction of the Hβ flux for underlying absorption in the stellar population was significant; we have applied an approximate correction based on typical values for synthetic stellar populations from Keel (1983).

The upper part in Table 4, with AGN-ionized gas detected more than 10 kpc from the nucleus, forms the sample for our subsequent analysis. As a sign of completeness, of these 19, 14 were found in both targeted and serendipitous searches. SDSS J095559.88+395446.9 was newly identified as a type 2 Seyfert in our spectrum, after having been found in the "blind" search of galaxies independent of prior classification as an AGN host (so it was not included in the targeted sample). Of the remainder, Mkn 78 and Mkn 463 were selected in the targeted AGN sample, while Mkn 1498 and UGC 11185 were recognized only in the serendipitous survey. It may be relevant that both Mkn 78 and Mkn 463 have ionized regions with relatively small projected extent, easily lost against the galaxy starlight (which in Mkn 463 is morphologically complex).

The [S II] $\lambda6717, 6731$ lines are particularly important, tracing electron densities and thereby providing one estimate of the intensity of the impinging ionizing radiation. Since the densities in these extended clouds are low, and the ratio is generally near its low-density limit, where the mapping from line ratio to density is highly nonlinear, we have examined the errors in measuring the line ratio closely. We generated multiple realizations of pixel-to-pixel noise, and each was scaled to four representative fractions of the stronger line peak. This was added to line pairs, modeled to match the line widths and pixel separation of the red Lick data. Gaussian fitting of the lines with added noise gave a relation between the peak signal-to-noise and error of the fitted ratio which we adopted; we use $\pm2\sigma$ error bounds to derive bounds on the density. Density values were calculated using the IRAF task *temden*.

3 ENERGY BUDGET IN EXTENDED CLOUDS: OBSCURATION VERSUS VARIABILITY

Seeing the effects of radiation from an AGN on gas tens of kpc from the nucleus allows us the possibility of tracing dramatic changes in core luminosity. One straightforward way to approach this question is a simple energy balance. The spectra give us upper and lower bounds on the required ionizing luminosity. To probe the most extreme conditions, we analyze galaxies in which we detect ionized gas at projected distances $r > 10$ kpc. For all distances and luminosities, we use the WMAP "consensus" cosmological parameters, with $H_0 = 72$ km s^{-1} Mpc^{-1} (Spergel et al. 2007).

The lower bound comes from the highest recombination-line surface brightness we observe; the central source must provide at least enough ionizing photons to sustain this over periods longer than the recombination timescale (which may be as long as 10^4 years at these low densities). This is a lower limit, since the actual emission-line surface brightness of some regions may be smeared out by seeing, and we do not know that a given feature is optically thick at the Lyman limit. This limit depends only very weakly on the slope of the ionizing continuum, since helium will generally absorb most of the radiation shortward of its ionization edge leaving only the 13.6-54.4 eV range to consider for hydrogen ionization. We base our bounds on the highest implied luminosity among structures at various projected radii in a given system, with no correction for projection effects. This makes our limits conservative, since a given cloud will always lie farther from the nucleus than our projected measurement. In essence, this argument is based on the surface brightness in a recombination line; we use Hβ since we have these data for the whole sample. In a simple approximation, we take the surface brightness in the brightest portion of a cloud, assuming this to be constant across the slit. We take the region sampled in this way to be circular in cross-section as seen from the nucleus, so its solid angle is derived from the region subtended by the slit. We then see this region occupying a small angle $\alpha = 2\arctan(\text{slit halfwidth}/r)$ as seen projected at angular distance r from the AGN, the required ionizing luminosity is given from observed quantities as $L_{ion} = 1.3 \times 10^{64} z^2 F(H\beta)/\alpha^2$ for α in degrees. The derived values are listed in Table 6, along with complementary quantities related to the nuclear luminosity (as collected below). The derived ionizing luminosities are lower limits, since there may be unresolved regions of higher surface brightness, and we do not know whether a given cloud is optically thick in the Lyman continuum. Higher-resolution imaging in the emission lines could this increase these values.

Upper limits to the incident ionizing flux come from a complementary analysis using the ionization parameter (U, the ratio of ionizing photons to particles), since these emission-line features all have [S II] line ratios near the low-density limit. Our density results from the $\lambda6717/\lambda6731$ [S II] line ratio are given in Table 7. Values are listed only for objects with useful measures far from the core. In each case, we evaluated the density at a typical temperature of 10^4 K, and at the higher temperature 1.3×10^4 K found in Hanny's Voorwerp (Lintott et al. 2009) and in our data for Mkn 266 and SDSS 2201+11, as set by thermal equilibrium for substantially subsolar oxygen abundance. We quote the extreme
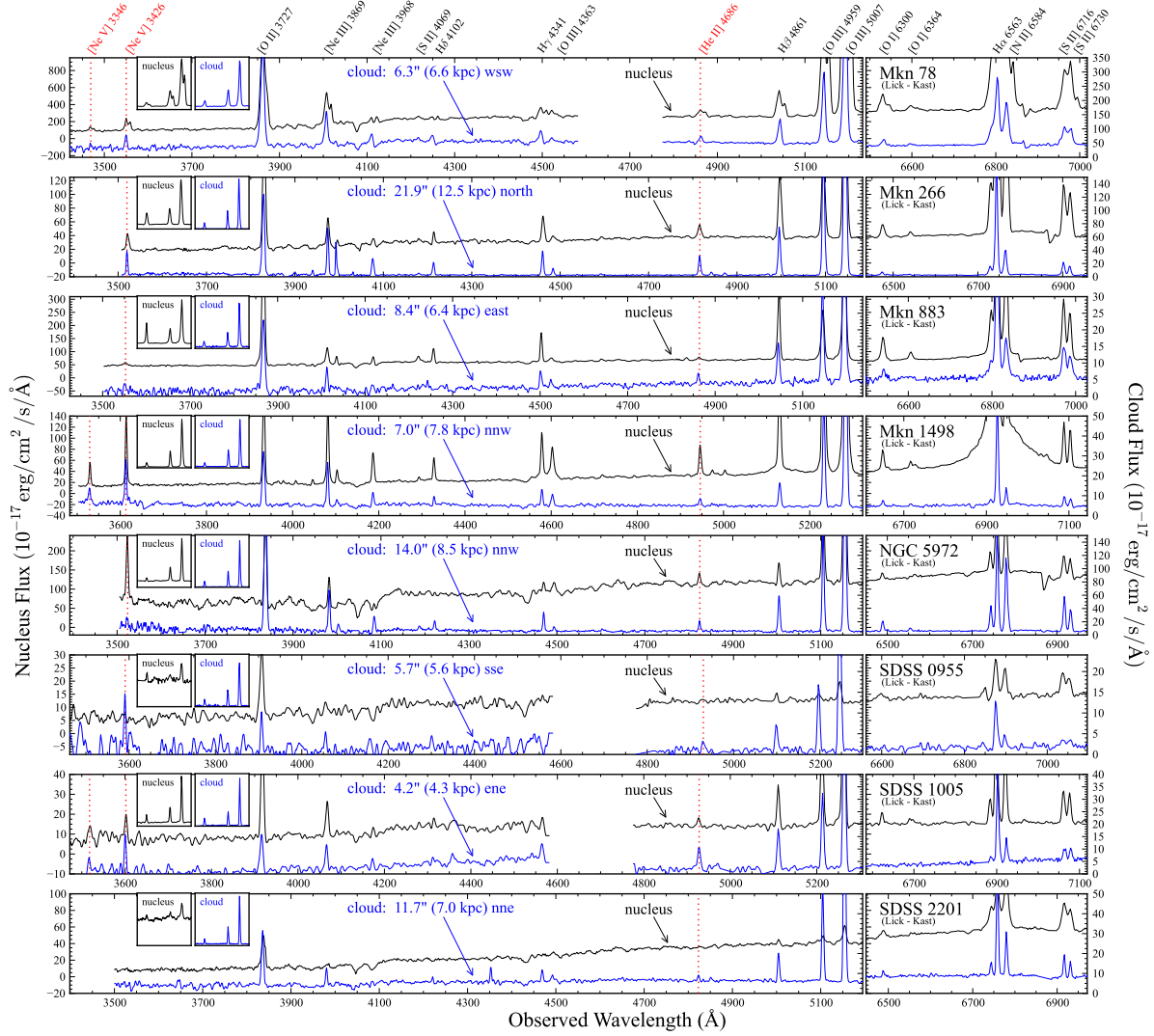
Figure 5. Lick spectra for nuclei and associated AGN-ionized clouds. Small insets at left show the Hβ+[O III] region for nuclei and clouds, scaled to the peak of λ5007 emission. Panels on the right show the [O I] - [S II] region at the same flux scale as the blue spectra. He II and [Ne V] emission, especially important as indicators of a hard ionizing radiation field, are indicated by red dotted lines when clearly detected in clouds. Nuclear spectra represent 2×3.1-arcsecond areas, and cloud spectra are summed over 2×6.2-arcsecond areas. Distances and directions of cloud relative to nuclei are indicated as shown. Three spectra have gaps in the blue region, since they were taken with the dichroic splitting red and blue optical trains near 4600 Å .

range of density values between these two cases (allowing in the Teacup an upper bound on the electron density as high as 240 cm^{-3}, and in some cases limits < 10cm^{-3}), since the temperature-sensitive [O III] $\lambda 4959 + 5007/\lambda 4363$ line ratio is not well-enough measured in most of these objects to use individual T_e values. We derive U from the [O II] $\lambda 3727$/[O III] $\lambda 5007$ ratio using the power-law continuum models from Komossa & Schulz (1997), and the analytic fits from Bennert (2005) as interpolation tools. For fully ionized hydrogen at a distance d from the AGN, the photon flux in the ionizing continuum is $Q = 4\pi d^2 n_e U/c$. For objects with red spectra, giving densities from the [S II] lines, limits to the luminosity

are given in Table 7. It is reassuring that the upper limits to ionizing luminosity derived from U and n_e always fall above the lower limits from recombination balance.

The lower limits from recombination-balance are independent of assumptions about the local density n_e, making it more robust than ionization-parameter arguments when we have no independent tracer at these low densities. Fig. 7 shows several of our objects in one of the "BPT" diagrams, going beyond their initial use to classify the gas as AGN-ionized to examine changes with projected distance from the nuclei. Some of these, such as Mkn 1498 and the Teacup 1430+13, show a phenomenon remarked earlier in,
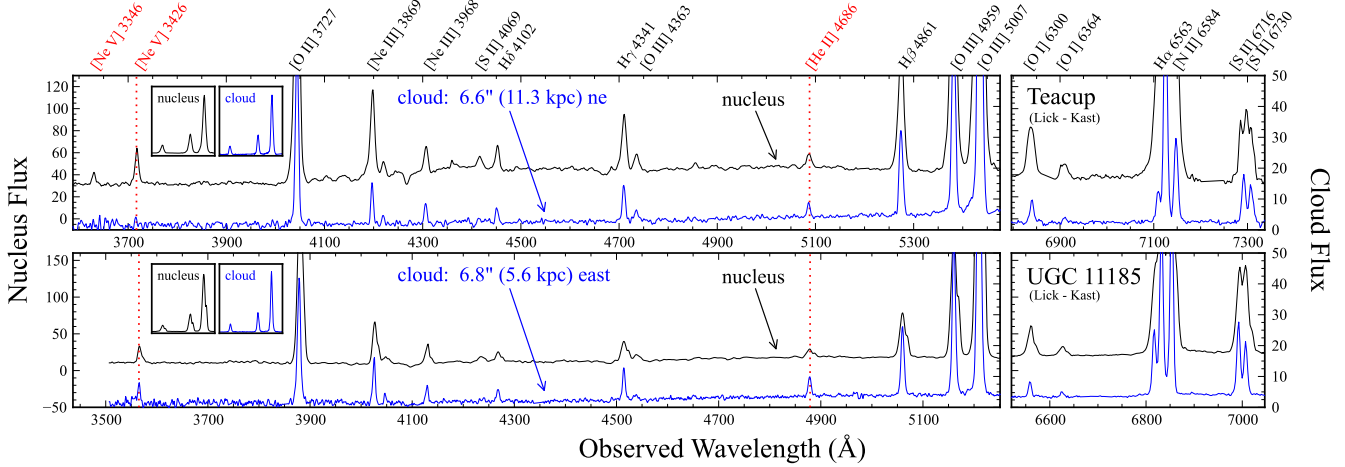
Figure 5 – *continued*

for example, NGC 5252 (Dadina et al. 2010) - the ionization balance stays roughly constant with radius, which is naturally explained if the characteristic density $n_e \propto r^{-2}$. This might occur naturally for gas in the host galaxy; tidal streams of gas would not be likely to match the extrapolated behavior of gas within the galaxy and indeed we see some cases (Mkn 266, NGC 5972, SDSS 2201+11) with substantial radial changes in U. However, for Seyfert narrow-line regions, Bennert et al. (2006b) find a shallower density gradient $n_e \propto R^{-1.1}$, which would imply $U \propto R^{-0.9}$ for gas which is optically thin (or has a small covering fraction). These objects have heterogenous behavior; In the ionization cone of NGC 7212, Cracco et al. (2011) find no radial trend of n_e.

Similar conclusions come from the more limited blue-line diagram also considered by Baldwin, Phillips, & Terlevich (1981), which we can apply to the objects for which we have only blue-light spectra from KPNO. Some of objects in this diagram as well as in Fig. 7 show systematic changes in ionization level with radius, manifested as offsets from upper left (higher ionization) to lower right (lower ionization). We show this behavior in Fig. 8.

We use far-IR data to estimate (or limit, for nondetections) the amount of AGN radiation absorbed (and reradiated) by nearby dense material, whether in an AGN "torus" or in the inner parts of the host interstellar medium. The FIR luminosity is conservatively high as an estimate of the potential obscured AGN luminosity, since there may be a nontrivial contribution from star formation in the host galaxy as well as the AGN, and in some cases companion galaxies might blend with the target in the FIR beam. In a simple picture where a fraction f of the AGN radiation is absorbed by nearby dust and reradiated, the FIR luminosity will be of order $L_{ion}f/4\pi$, with an additional scaling factor of a few to account for non-ionizing radiation heating the grains (which we omit at this point for the sake of a conservative calculation). For convenience, we approximate the total far-IR output by the FIR parameter introduced for IRAS point-source catalog data (Fullmer & Lonsdale 1989), a linear combination of flux values in the 60 and 100μ bands which gives a reasonable approximation to the total flux be-

tween 42-122μ. Numerically,

$$\text{FIR(W m}^{-2}) = 1.26 \times 10^{-14}(2.58f_{60} + f_{100})$$

for *IRAS* fluxes in the 60 and 100 μ bands given in Jy (multiplied by 10^7 for a result in ergs cm^{-2} s^{-1}). *IRAS* data were supplemented, where possible, by *Akari* data (Murakami et al. 2007, Kawada et al. 2007, Yamamura et al. 2010) of higher accuracy. The positions of all these galaxies were covered in the *IRAS* survey, so we can assign typical upper limits to nondetections depending on ecliptic latitude; *Akari* added two additional detections not found in the IRAS data, using only quality 1 (confirmed detection) fluxes. For non-ULIRG objects ($L_{FIR} < 10^{45}$ erg s^{-1}), we can reproduce the *IRAS* FIR parameter from *Akari* 90μ fluxes and mean colours via

$$\text{FIR(W m}^{-2}) \approx 5.0 \times 10^{-14}f_{90}$$

with 30% accuracy (± 0.15 dex), and we use this to fill in FIR luminosities for the objects detected only by *Akari*. The input values and results of this energy-balance test are shown in Table 6. Within our sample, Mkn 273 and Mkn 266 are classic ultraluminous infrared galaxies (ULIRGs), with $L_{FIR} = 1 - 5 \times 10^{45}$ erg s^{-1}. Some of the others remain undetected in both the IRAS and *Akari* surveys, leading to limits typically $< 10^{44}$ erg s^{-1}. An index of whether the extended clouds can be ionized by an obscured AGN is provided by the ratio of required ionizing luminosity to FIR luminosity, tabulated in Table **??**. These values are all lower limits, since the ionizing luminosity is a lower limit This ratio ranges from 0.02 to values > 12 (FIg. 9). Low values clearly represent AGN which are strongly obscured along our line of sight but not toward the EELR clouds. Large ratios indicate long-term fading of the AGN, a spectral shape strongly peaked in the ionizing UV, or very specific geometry for obscuring material, and thus indicate objects worthy of close attention.

Arguments for long-timescale variations in the central sources here depend on our having estimates for their total luminosity as seen directly, which could in principle fail either if their ionizing radiation were collimated by something other than obscuration, or the spectral shapes in the deep
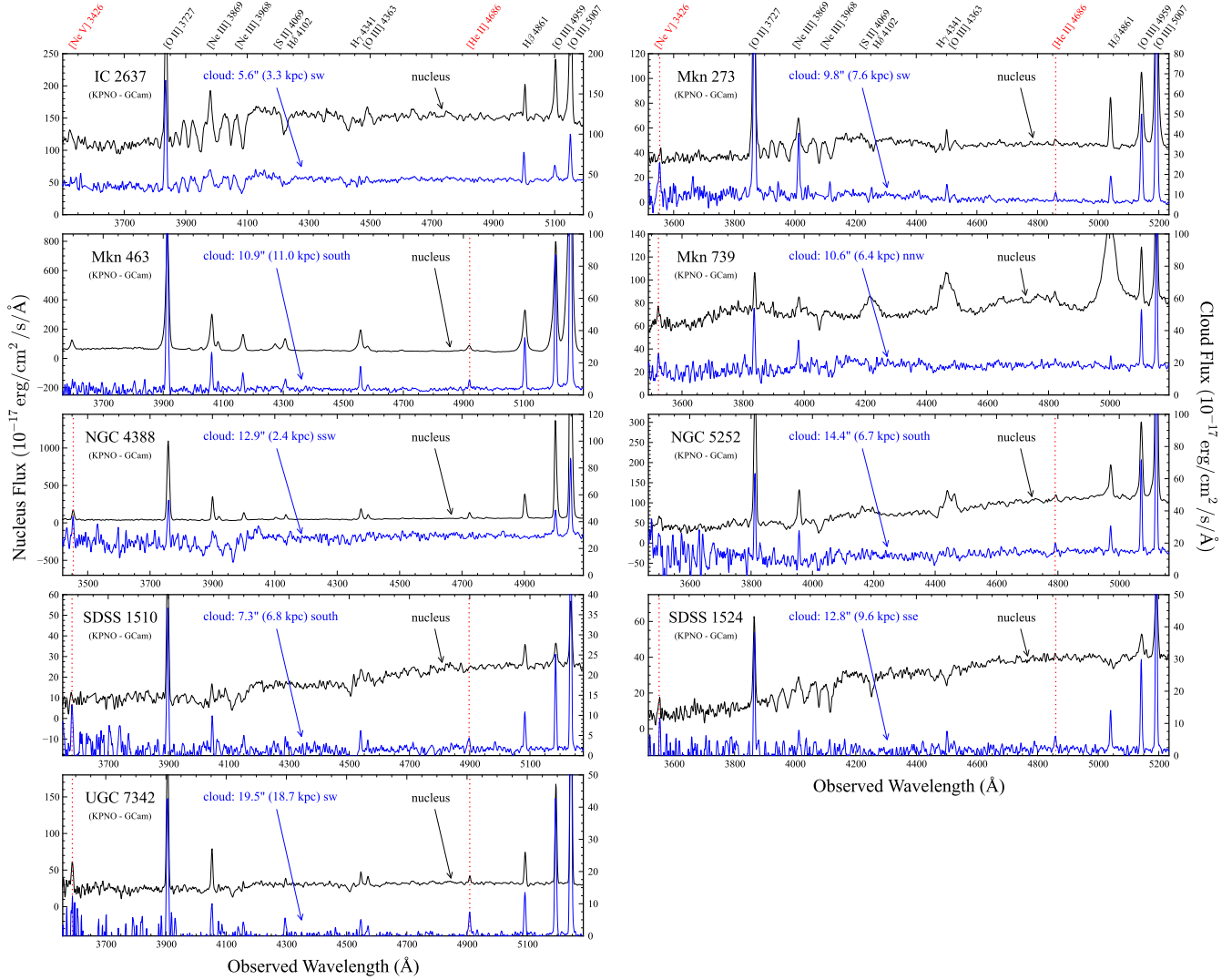
Figure 6. KPNO GoldCam spectra sampling nuclei and associated AGN-ionized clouds. Spectra are scaled to show [O III] $\lambda 4959$, with nuclear spectra representing 2×3.1-arcsecond areas and cloud spectra representing 2×6.2-arcsecond areas. He II and [Ne V] emission, especially important as indicators of a hard ionizing radiation field, are indicated by red dotted lines when clearly detected in clouds. Distances and directions of cloud relative to nuclei are indicated as shown.

ultraviolet differ from our expectations based on the UV and X-ray behavior of familiar AGN. Collimation by relativistic beaming does not fit the combinations of opening angle and flux ratio is required (as found for Hanny's Voorwerp; Keel et al. 2011). A spectral solution to the behavior would require an extreme-ultraviolet 'bump' dominating the ionizing flux from 13.6-54 eV by more than an order of magnitude. However, known AGN do not provide evident examples of either solution; the most straightforward interpretation of the data suggests that some of these clouds are ionized by AGN which have faded over the differential light-travel time between our views of the clouds and nuclei.

4 NUCLEAR AND EXTENDED RADIO EMISSION

To further characterize the AGN in these galaxies, we collected radio fluxes at 1.4 GHz from the NVSS source catalog

(Condon et al. 1998). All but two objects (SDSS 1510+07 and 1005+28) were detected above the 2.5 mJy survey limit; the source luminosity L(1.4 GHz) ranges from $< 1.3 \times 10^{22}$ W Hz^{-1} to 2.0×10^{24}, the latter for the double source associated with NGC 5972 and comprising 94% of the galaxy's total flux. Eight of the galaxies qualify as radio-loud if one uses a simple, representative division at 10^{23} W Hz^{-1}, and only one lies above 10^{24}. This one - NGC 5972 - represents an interesting departure from the usual alignment of emission-line and radio structure (section 7).

5 HOST AND CLOUD MORPHOLOGY

The examples of Hanny's Voorwerp (Josza et al. 2009) and NGC 5252 (Prieto & Freudlng 1996) suggest that a common source of extraplanar gas at large radii is tidal debris. The host morphologies of the galaxies where we find extended ionized clouds support this notion. Table 8 lists morpho-
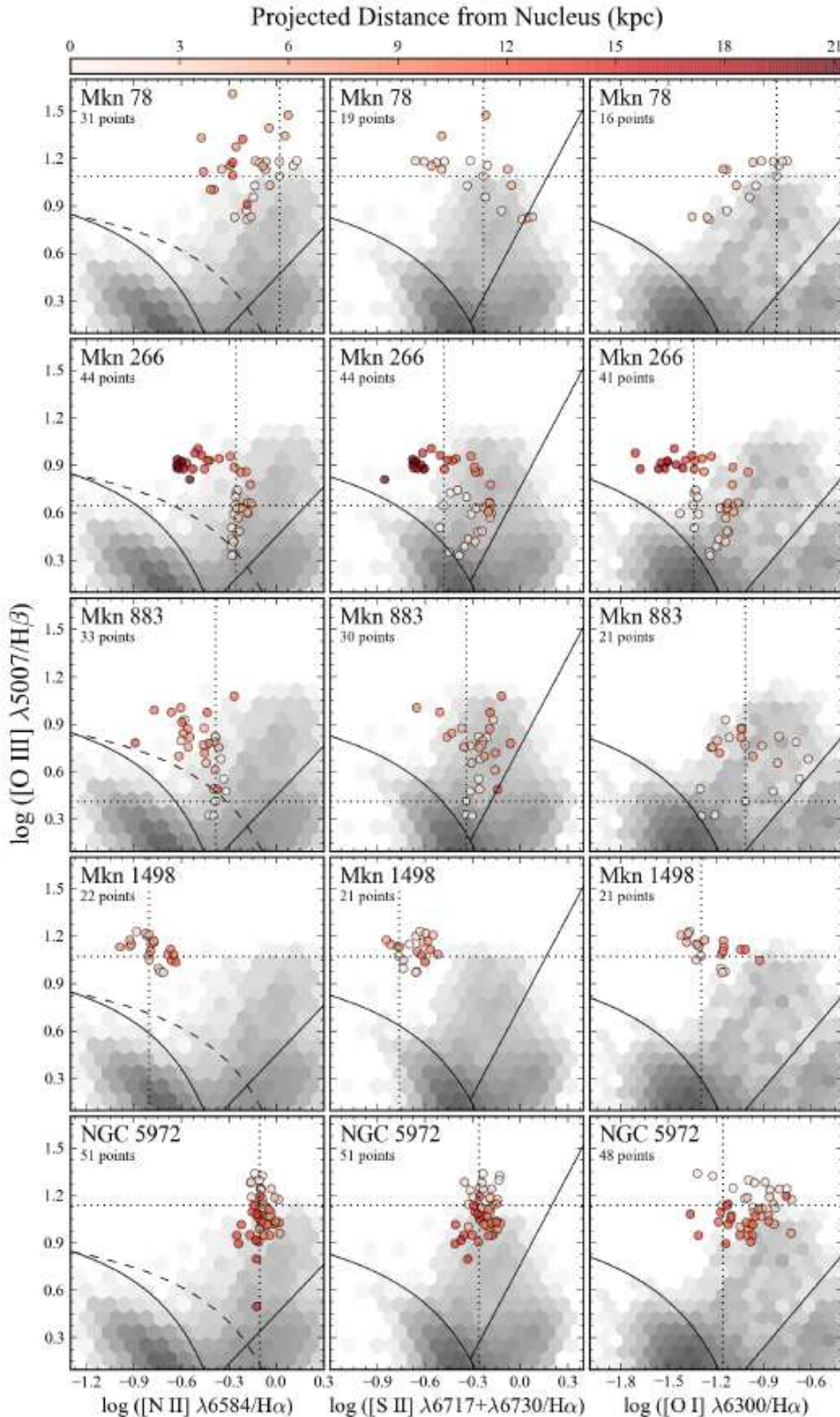
Figure 7. Baldwin-Phillips-Terlevich (BPT) diagrams for spatial slices in Lick data. Each row shows the three classical BPT diagrams for each object, highlighting radial ionization behaviors. The nucleus is indicated by crosshairs, with colors changing from white to red with increasing distance from the nucleus. The greyscale background and dividing lines are the same as in Figure 4; these show only the region around the AGN loci in each case for discrimination of detail. Nearly all measurements lie firmly in the AGN domain, with possible exceptions in some regions of SDSS 1005 and SDSS 0955. The starburst/AGN ionization boundary from Kewley et al. (2001) is shown as the red full curve, while the boundary from Kauffmann et al. (2003) is the black dashed curve. All these measurements lie firmly in the AGN domain, with the possible exception of two regions in SDSS 1005 and the nucleus of Mkn 883, whose red spectrum shows a broad-line region and strong [O I]. The greyscale show the density of points representing low-redshift galactic nuclei in the SDSS, from Schawinski et al. (2010b), which we also follow in adopting the straight line as the LINER/Seyfert boundary
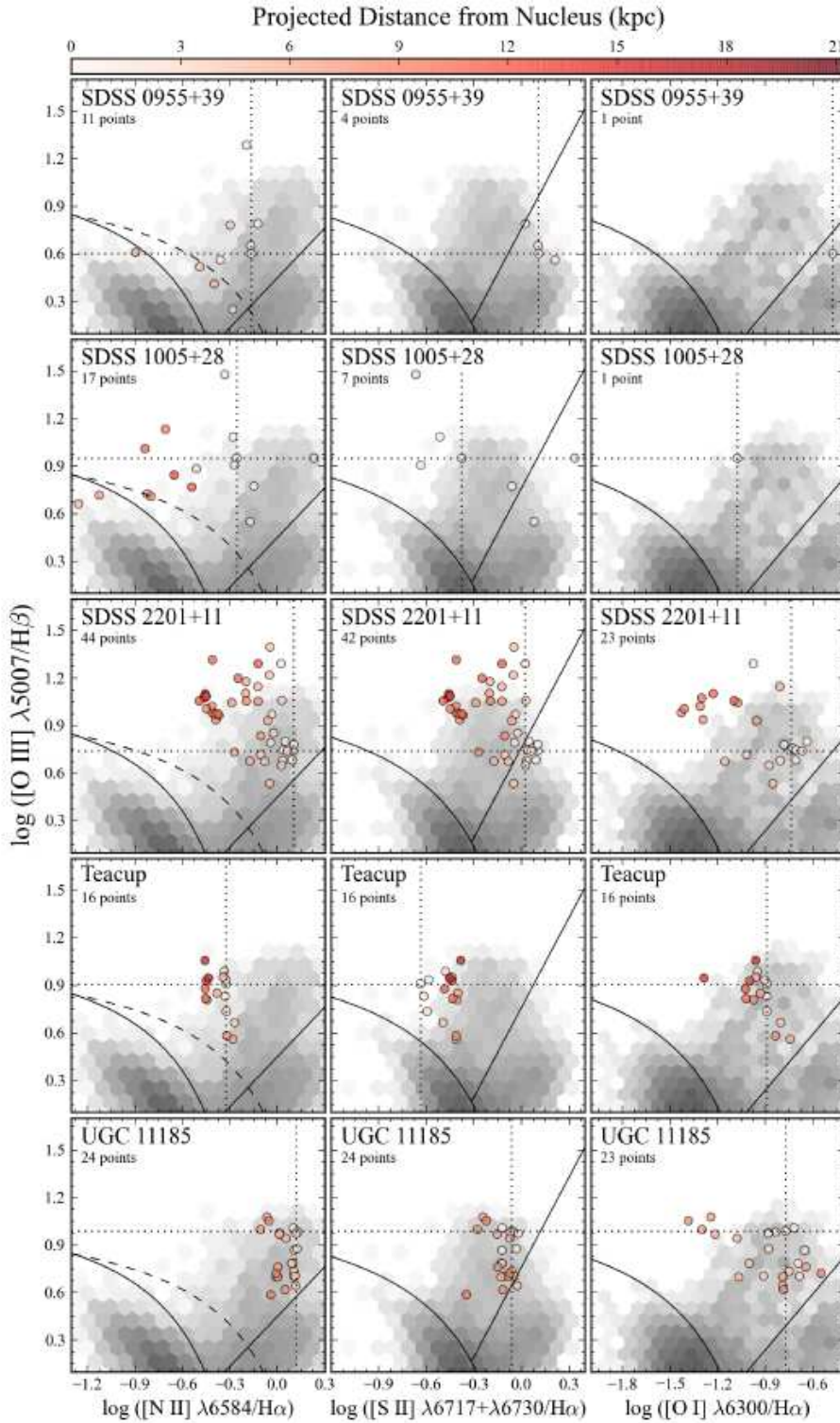
Figure 7 – *continued*

logical information on these galaxies, including warps, close companions, asymmetries, or ongoing mergers. The actual incidence of tidal structures will be higher - for example, the inclined ring of gas with distinct kinematics in NGC 5252 has no optical counterpart. Of the 19 confirmed large-scale clouds, 14 are in systems classified from SDSS data alone as interacting, merging, or postmerger (still showing tidal tails). This remarkably high incidence of disturbed systems (at least 73%, even without including NGC 5252) supports the idea that most very extended emission-line clouds around local AGN represent illuminated tidal debris. We illustrate this in Fig. 10, showing the SDSS colour images with

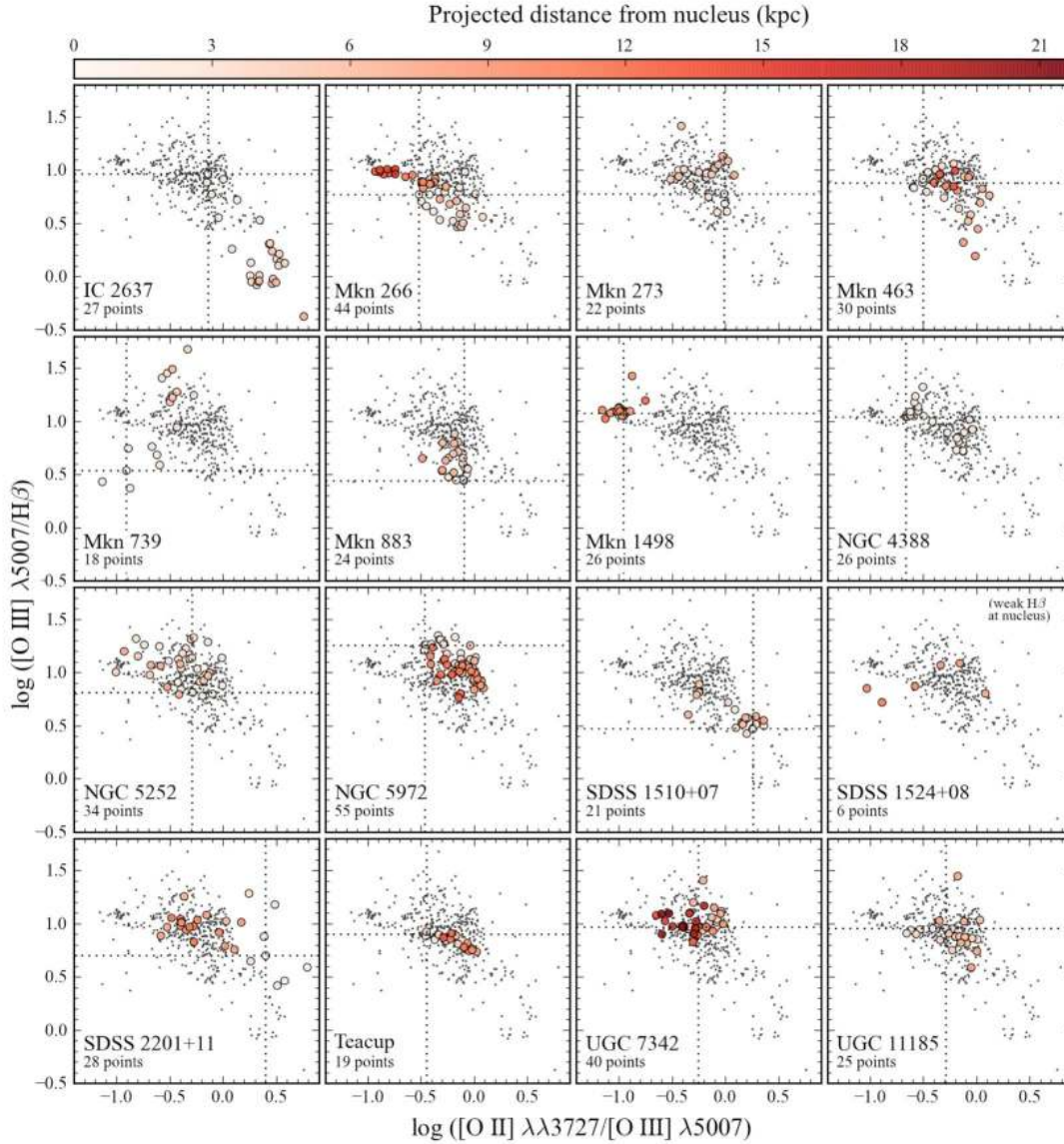**Figure 8.** An alternate Baldwin-Phillips-Terlevich (BPT) diagram, usable when only blue spectra are available (in this case, from the Kitt Peak GoldCam). As in Fig. 7, points are colour-coded with projected distance from the galaxy nuclei. Since Mkn 739 has a significant broad-line region, its Hβ components were deblended using a broad Gaussian and narrow Lorentzian, with narrow-line ratios plotted here.
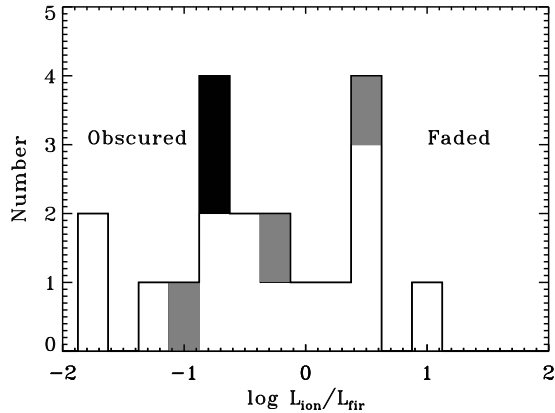
Figure 9. Distribution of the ratio L_{ion}/L_{FIR} in the log. Small values are consistent with AGN heavily obscured along our line of sight but not toward the emission-line clouds, while large values indicate fading of the AGN. Shaded regions show that there is no obvious differences in the distributions among type 1 Seyferts (black), intermediate type 1.5 and 19 objets grey), and type 2 nucle (white).

the *g*-band [O III] contribution enhanced to show the clouds' locations. In this section, we include IC 2497/Hanny's Voorwerp in the tabulations for comparison. A striking instance of a QSO ionizing gas in a companion and tidal tail, on similar scales $\approx$ 40 kpc, has been reported by de Silva et al. (2011).

Several of these galaxies show discs seen nearly edge-on. From these, it is clear that the ionizing radiation can emerge well away from the disc poles. The projected angles from stellar disc to the axis of the ionized clouds, when it is well defined, range from 30–54°. This fits with the statistics reported by Schmitt et al. (1997), in which obscured (type 2) objects show a wider range of angle than type 1 objects between the host-galaxy axes and the AGN axes as traced by radio jets.

We see both one- and two-sided emission regions. The two-sided regions are generally highly symmetric in angular location, although not necessarily in radial extent or surface brightness, fitting with biconical illumination patterns. As listed in Table 8, 9 of 19 of our confirmed objects have emission detected on both sides of the nucleus. Particularly in very disturbed systems, a strong asymmetry may reflect the location of cold gas rather than the pattern of escaping ionizing radiation, so that we cannot necessarily conclude that the one-sided clouds are in galaxies that do not have two-sided radiation patterns

The angular width of regions of escaping radiation may constrain the geometry of obscuring regions, if the ionization is bounded by the availability of radiation rather than gas. We list, in Table 8, a cone angle, which is the projected angular width of each half of a notional bicone encompassing all the high-ionization regions seen in our images, outside of a usual nuclear emission region (Fig. 11). Projection effects make the observed angle an upper limit to the three-dimensional opening angle of a cone. The sample of large emission clouds exhibits a wide range, from 23–112°. The narrower ones are challenging to understand from obscu-
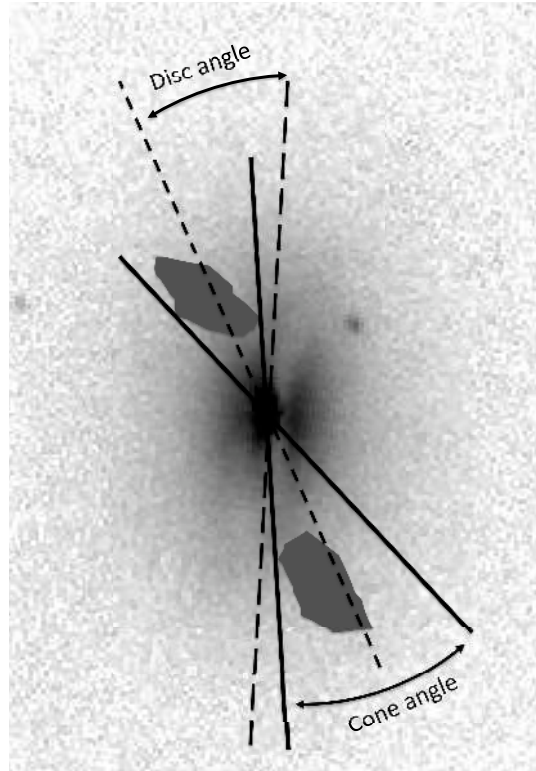

Figure 11. Illustration of angles listed in Table 8. The disc angle, defined only for highly inclined and reasonably symmetric host disks, is measured from the projected major axis of the disc to the midpoint of the cloud (bi)cones. The cone angle, as shown, measures the width of the paired triangles about the nucleus that encompass the extranuclear emission detected in available images. The base image is the SDSS *r* observation of SDSS 2201+11, with the [O III] clouds shown schematically.

ration by a circumnuclear torus, suggesting absorbers that are geometrically quite thick compared to the opening angle for escape of ionizing radiation, to an extent which might better be described as an obscuring shell with small polar holes. However, some of these objects have dual clouds in very symmetric locations, which would be most naturally explained by such a scheme.

Several of the two-sided clouds show near-symmetry in radial extent on opposite sides of the galaxy. This could reflect episodic activity on the light-travel time scale, although front-back geometric effects would generally break an exact symmetry.

6   KINEMATICS OF IONIZED GAS

Extended ionized regions around AGN may commonly be separated into kinematically quiescent components, such as would be seen for disk gas ionized from the nucleus, and outflow, with additional superimposed radial motion which might be manifested in a well-sampled velocity field as misalignment of the velocity field with the galaxy morphology if the superimposed velocity components are not spectrally
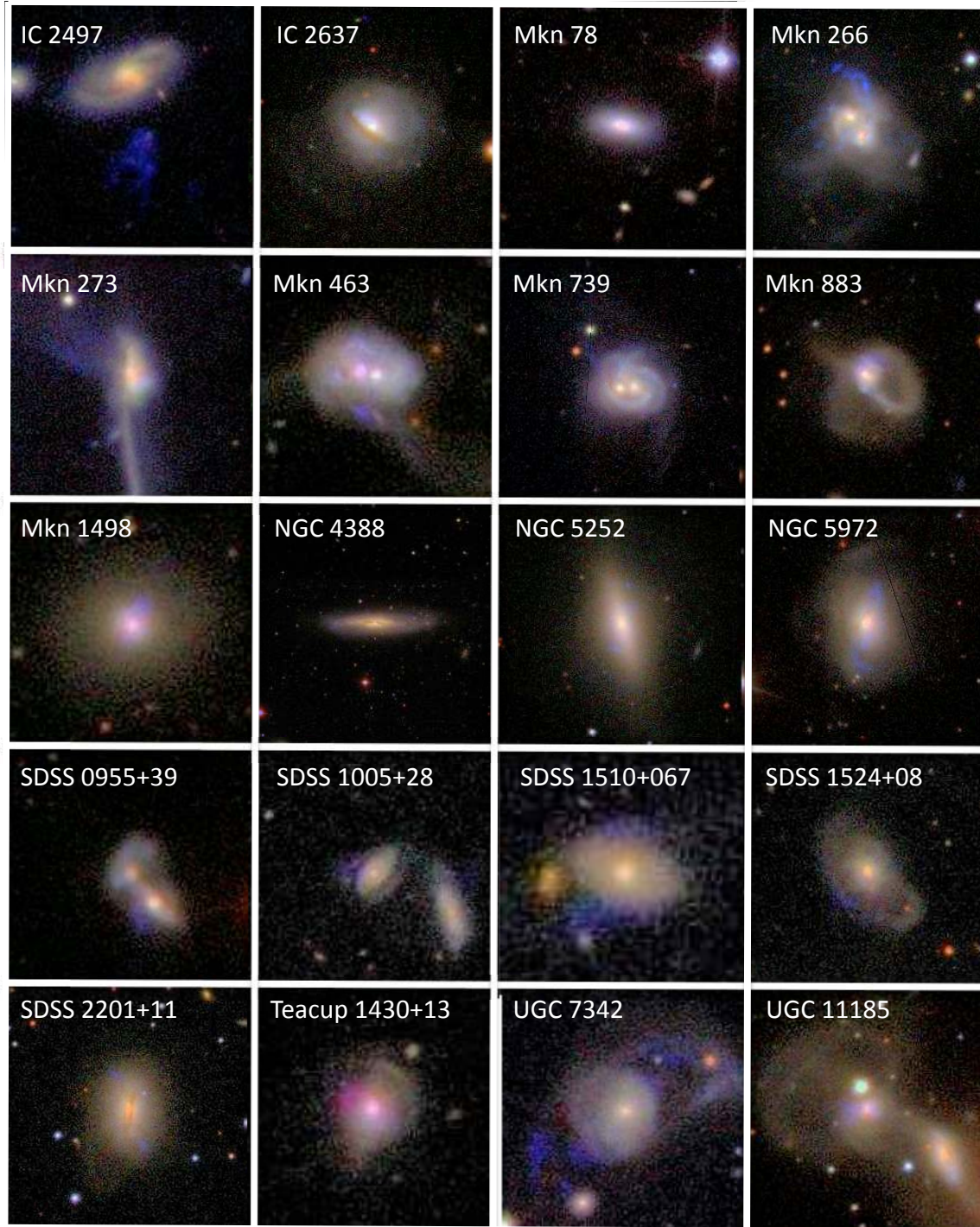
Figure 10. Host morphologies and ionized-gas structures in the Galaxy Zoo sample of AGN-ionized clouds. These are based SDSS colour image products, with *gri* filters mapped to BGR for display. However, to enhance visibility of the ionized clouds, the contrast of the *g* filter has been increased in this figure, across the intensity ranges needed to show the gas effectively. Each image cutout spans 70×70 kpc with north at the top. As in Table 8, IC 2497 is included for comparison.

resoved (Barbosa et al. 2009). In addition, for disturbed systems, tidal features may show motions decoupled from the disk itself. We consider here the information on gas kinematics provided by our spectra, noting that in most cases we sample only a single position angle through each galaxy.

Redshifts were measured for each pixel along the slit using Gaussian fitting in IRAF. We show results for [O III], Hβ, and when observed, Hα and [N II]. Velocity errors are based on propagation of photon statistics (Keel 1996).

Fig. 12 shows a selection of these velocity slices, relative to the nucleus in each case. Despite the angular offset from the edge-on disk, the gas velocities in SDSS 2201+11 are continuous with the pattern in the inner rotating section, and closely symmetric. Similarly, the emission clouds in NGC 5972 fall along an extrapolation of the inner-disk rotation curve (as traced by [O III]). Despite its very disturbed morphology, UGC 11185 shows near-symmetry in kinematics, with a very strong velocity gradient crossing the nucleus.

Other systems in our sample show less ordered velocity slices. The gas in UGC 7342 at all radii has a single sense of motion on each side of the nucleus, but local departures have amplitudes up to 120 km s^{-1}. A central gradient in the Teacup (SDSS 1430+13) may be reversed where the slit crosses its loop of emission. The kinematics in Mkn 883 and Mkn 739 are very disordered, as expected for a merging system. In Mkn 78, multiple components are seen in the inner few arcseconds, even in [Ne V] (Fischer et al. 2011).

The northern filament in Mkn 266 presents interesting kinematic behavior, with a large and consistent velocity offset between [O III] and Hα, Hβ. This difference is seen in spectra from both spectrographs. A likely explanation is superposition of structures with quite different ionization states as well as velocity, so that the weighting of lines in our spectra, even though they are not separately resolved, gives different velocity centroids. The offset is close to 50 km s^{-1} along the entire filament. Localized instances of similar mismatches between [O III] and Hβ velocities on one side of SDSS 2201+11 and possibly in NCG 5972. Outflows are typically inferred from blue wings on [O III], but far from the nuclei where disk extinction is unlikely to be a major effect, velocity offsets of either sign could show outflows. One corollary of this distinction is that there exists a gas component of much higher excitation than implied by the ionization parameter we derived from ratios of total line flux at these locations, suggesting higher ionizing luminosities in these galaxies.

The relatively quiescent kinematics of most of these features may indicate a contrast in origin of the extended gas when compared with the radio-loud QSOs (Fu & Stockton 2009a, Fu & Stockton 2009b). In their sample, modest star-formation rates led them to suggest that much of the ionized gas was expelled from the system by the launch of powerful radio jets. The galaxies in our EELR sample are mostly radio-quiet (or at least radio-weak), as noted above. Also unlike their QSO sample, we see significant metallicity differences between the nuclei and EELRs, most strongly shown in the [N II]/Hα ratio, again consistent with the EELR gas having an external tidal origin.

7 NOTEWORTHY SYSTEMS

From our results or previously reported data, several of these galaxies have interesting individual features.

The inner parts of the EELR in Mkn 78 have long been known (Pedlar et al. 1989, who detected much of the [O III] extent we observe), and observed with HST in both imaging and spectroscopic modes (Capetti et al. 1994, Whittle & Wilson 2004). A detailed fit to the HST radial velocities explains the double line profiles near the core without requiring a second AGN (Fischer et al. 2011); optical and near-IR line spectra suggest that the gas is photoionized from the nucleus with at most a very localized role for excitation by interaction with small-scale radio jets (Whittle et al. 2005, Ramos Almeida et al. 2006). Our data also show the complex spatial and velocity structure in the inner few arcseconds. The outer emission is spatially smooth, and is measured to much larger radii in our spectra than in the initial SDSS imaging detection.

In Mkn 883, the blue line ratios indicate that it lies near the Seyfert/starburst boundary. Only in the red do weak broad Hα and [O I] definitely indicate an AGN. We do not detect a broad component at Hβ.

For NGC 4388, the SDSS images detect only a few inner knots of the extensive emission region revealed by, for example, *Subaru* imaging Yoshida et al. (2002). Our spectra detect more of this structure. Our cone angle is estimated from the *Subaru* image. Detailed spectroscopy by Michitoshi et al. (2004) confirms that this distant gas is photoionized by the AGN.

NGC 5252 has been considered the archetypal Seyfert galaxy with ionization cones. The implied energetics of the nucleus depend critically on the density in the ionized filaments. Our implied limits from photoionization balance via surface brightness in Hβ are significantly greater than the values suggested from pressure balance with the galaxy's hot ISM (Dadina et al. 2010), while we concur with the X-ray results that the ionization parameter remains roughly constant with radius among the ionized features. In turn, the interpretation of this behavior depends on fine structure (much still unresolved) in the emission-line filaments, as seen in Hanny's Voorwerp (Keel et al. 2011).

Two objects in this sample appear to violate the usual pattern of ionization cones encompassing radio-source axes. NGC 5972 is the most radio-luminous of our galaxies, and shows a typical double-lobed structure Condon & Broderick (1988). The lobes are separated by 9.4' (330 kpc) in projection, and are oriented near PA 100°, quite different from the optical emission at PA 167°. In this source, the most radio-powerful in our sample, the very different geometries of the line and radio emission make ionization from interaction with the radio plasma unlikely, and their near-perpendicular orientation is unlike the typical case for Seyfert galaxies (Wilson & Tsvetanov 1994). This could be explained if the ionization cones have extremely broad opening angles, or if the radio structure makes a dramatic and yet-unobserved twist on small scales. Similarly, Mkn 1498 is associated with a giant low-frequency double radio source Röttgering et al. (1996), with projected separation 1.1 Mpc. In this case as well, the orientations of the emission-line structures and the large radio source differ strongly, by about 70°.

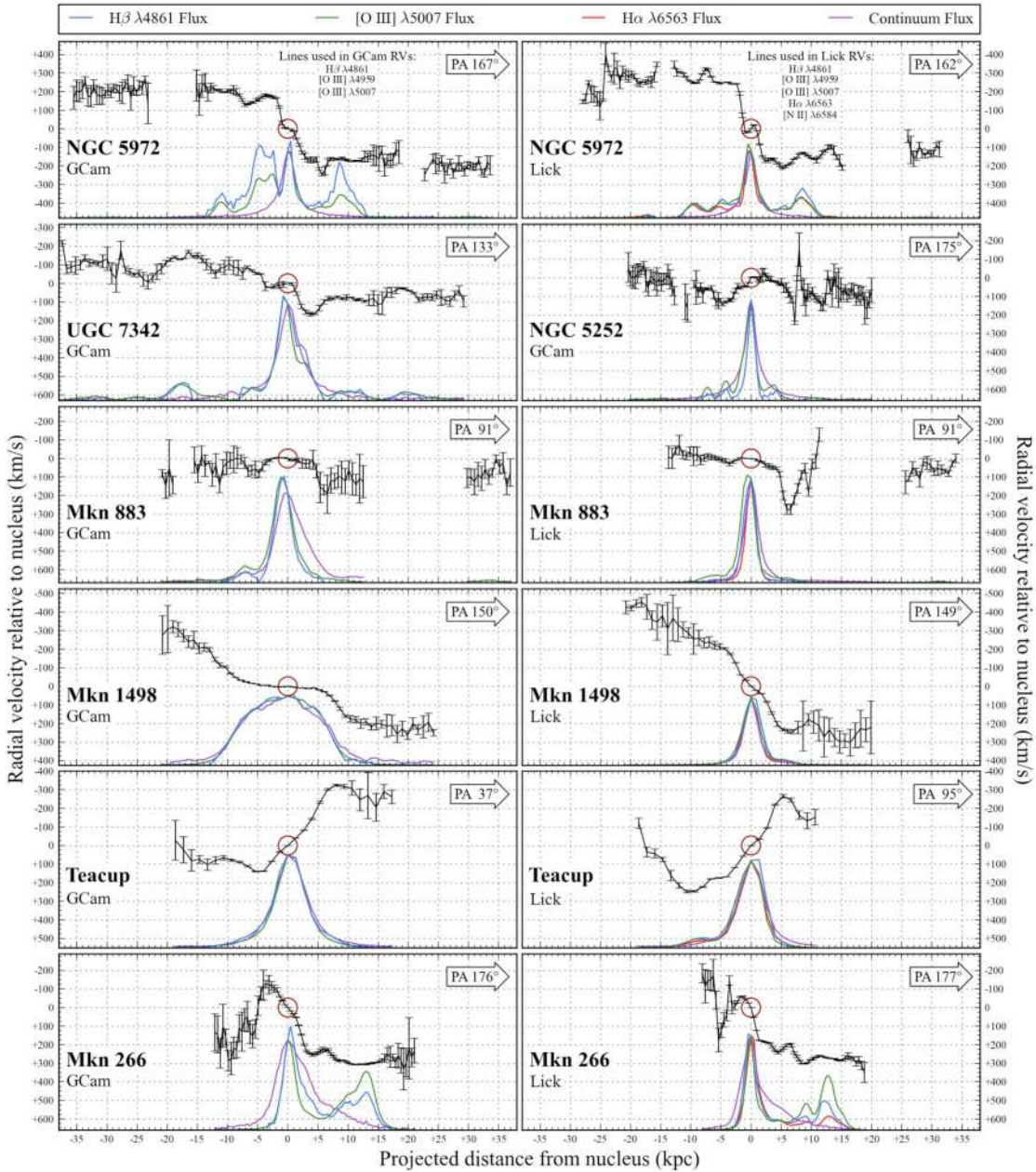SDSS 1430+13, the "Teacup" AGN, is distinguished by

Figure 12. Radial-velocity slices (shown relative to the nuclei) along our slit locations for selected hosts and AGN clouds. Nuclei are indicated by dark red circles. Lines used in calculating radial velocites from GCam and Lick data sets are indicated in the plots for NGC 5972, one of several objects observed at both locations though typically at slightly different position angles. In some cases, the extended emission follows the inner rotation closely even for extraplanar gas, as in SDSS 2201+11 and NGC 5972. Others are more chaotic, as expected for mergers. Particularly for Mkn 266, some structures show significant differences between the lines, indicating that we are seeing blends of multiple components with very different line ratios. Intensity slices in the continuum and lines are plotted across the bottom to show correlations between location and velocity structure, scaled in flux to match [O III] λ . Velocity errors are calculated as $\pm 2\sigma$ from photon statistics following Keel (1996); in some cases, larger errors may be appropriate from such factors as blending of multiple components.
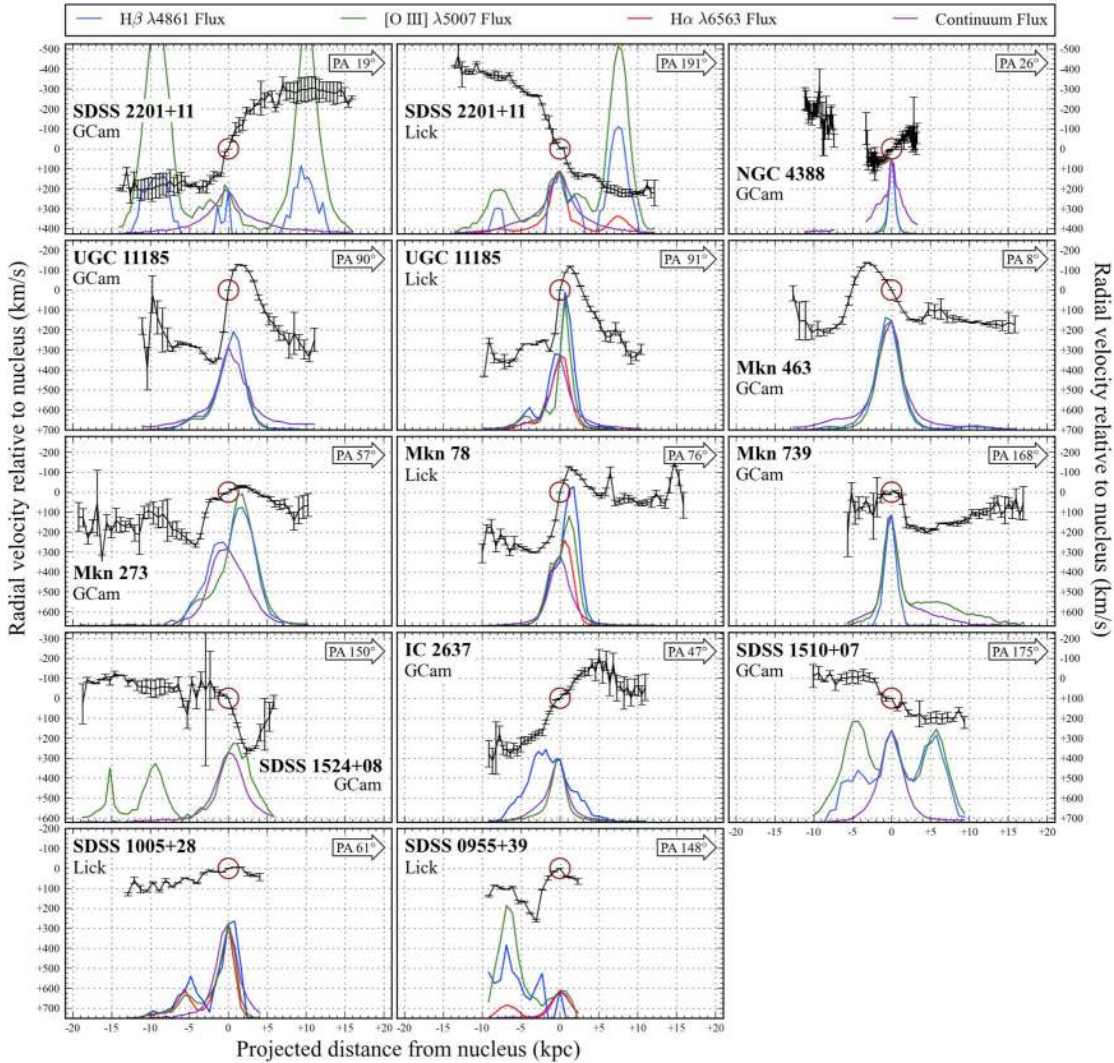
Figure 12 – *continued*

a 5-kpc loop of ionized gas. The FIRST VLA data at 20 cm show extended structure roughly coextensive with this feature, possibly indicating a related origin.

In both SDSS 2201+11 and SDSS 1111-00 (the latter observed spectroscopically but with emission smaller than our 10-kpc limit), the extranuclear clouds outshine the AGN itself in the [O III] lines.

UGC 11185 shows a second, weaker set of emission-line components near the nucleus, peaking about 1.8" to the east along our slit, roughly 600 km s^{-1} to the red of the main

peaks, and including about 1/4 of the nuclear [O III] flux within a 2×3" aperture.

In both Mkn 463 and Mkn 739, *Chandra* imaging has furnished evidence for double AGN (Koss et al. 2011, Bianchi et al. 2008). In both cases, the emission regions are much larger than the separation between AGN components, so we do not know whether the ionization is associated mostly with one or the other. More detailed [O III] images could resolve this. However the flux sources are apportioned between components, one AGN in each system must have an ionizing/FIR ratio at least as high as our tabulated limit. Several earlier studies have noted the extended [O III] emission around Mkn 463 (Mazzarella et al. 1991, Uomoto et al. 1993, Chatzichristou & Vanderriest 1995).

Wu et al. (2011) summarize polarimetric detections of "hidden" broad-line regions in nearby AGN. Their list includes four of the nuclei in our sample: NGC 4388, NGC 5252, Mkn 78, and Mkn 463. Broad wings to the Balmer lines are seen in Mkn 266 (southwestern nucleus) and Mkn 739 (eastern nucleus), making them clear Sy 1 nuclei with "non-hidden" broad-line regions. Weak wings are seen at Hβ in Mkn 1498, which would then be classified as a type 1.8 object (Osterbrock 1977).

8   CONCLUSIONS

Volunteers in the Galaxy Zoo project have carried out a search for AGN-ionized gas clouds on large scales (10-40 kpc). This paper has documented the search, and spectroscopic observations of candidates yielding 19 such features. These clouds were classified as AGN-photoionized based on their locations in the Baldwin-Phillips-Terlevich (BPT) line-ratio diagrams, strength of [Ne V] and He II emission, and (when measurements are sufficient) modest electron temperatures $T_e < 20,000$ K, consistent with photoionization but not with shock heating. Most of the host galaxies show signs of interaction, suggesting that the extended ionized gas in many cases rises from tidal tails.

We consider upper and lower bounds to the luminosity of the AGN as it reached the clouds - lower limits from recombination and upper limits from density and ionization parameter. We compare these with the obscured luminosity estimated from far-infrared measurements; an excess in ionizing luminosity (or deficit in the far-IR) could signal long-term variability of the AGN. The ratio of ionizing to obscured luminosity spans a wide range, from 0.02 to > 12. Over a third of them (7/19) exceed unity, making this kind of energy deficit a common issue. Small values fit with an origin in obscured AGN, requiring only a small fraction of the extreme ultraviolet to escape. In contrast, large values may require a long-term fading of the AGN. An extreme case of this is represented by Hanny's Voorwerp near IC 2497 (Lintott et al. 2009). In this object, the required ionizing flux indicates that the AGN has faded by a factor > 1000 within the last $\approx 2 \times 10^5$ years, sampling a timescale on which we otherwise have no information. More detailed observations of this new sample, including pending X-ray measurements, could give statistics adequate to show how common such variations are.

An important use of this sample is in addressing the history of AGN luminosity - on what timescales do episodes of

high luminosity persist and fade? Broad arguments suggest that AGN episodes extend over spans comparable to the duration of a galaxy merger (several 10^8 years), if statistics associating excess AGN with strong interactions and mergers are representative. We note that establishing a link between galaxy interactions and AGN episodes has proven remarkably elusive, with the results depending on details of comparison sample selection and what kind of AGN is studied; as recent examples, Maia et al. (2003), Alonso et al. (2007), and Li et al. (2008) reached different conclusions - a null result, enhancement limited to certain kinds of AGN, or a weak overall enhancement of AGN - from similar analysis of nearby galaxy samples. Therefore, even within such long timespans, we have little information on how episodic the accretion and associated luminous output might be.

The relevant equation for time delay between radiation reaching us directly from the nucleus and that reprocessed in a cloud follow usage for light echos in ordinary reflection, except that here we are constrained by the location of gas so we deal with a constant observed radius r_{proj} and unknown angle θ between the illumination direction and the plane of the sky; and the long recombination times at low density impose a convolution with a nontrivial time span for response. With the geometry defined in Fig. 13, keeping r_{proj} fixed by the observations means that the geometrical time delay Δt for observing reprocessed nuclear radiation depends on the the viewing angle θ (from observer to nucleus to the cloud, with a cloud along the line of sight at zero and increasing away from the observer) as given by

$$\Delta t = \frac{r_{proj}}{c \sin \theta}(1 - \cos \theta) \qquad (1)$$

derived in the approximation of infinite distance from the observer. Two-sided symmetric sets of clouds have progressively much longer differential delays when seen with their axis near the line of sight, so that a faded source in this regime should eventually be seen ionizing only the farside cloud. Our ability to reconstruct the actual distribution of θ is hampered by an inner cutoff in r_{proj} (10 kpc, so that the cloud detection is not hampered by galaxy starlight) and lack of knowledge of the distribution of cloud extent from the nuclei. To be conservative, our calculations of ionizing luminosity (above) assume $\theta = 90°$, the minimum possible distance for the nucleus and thus minimal ionizing luminosity,

We might expect our sample to be complete at least for the lowest redshifts and highest surface brightnesses, but there are a few objects with selection priority as high as some of our cloud hosts for which we do not yet have confirming optical spectra. Of our 19 confirmations, 14 were found in both the targeted and serendipitous searches. Two were found only in the targeted search, and 3 in the serendipitous search. Of these 3, one (SDSS J095559.88+395446.9) had no previous optical spectrum and could not have been included in the targeted sample.

A first hint as to characteristic timescales comes for the relative numbers of galaxies with and without deficits in ionizing luminosity, since the ones with deficits in the energy budget would be seen during the appropriate delay time after fading of the nucleus. There is no obvious reason for this ratio to be biased in our sample, since the serendipitous survey was independent of the presence of an AGN, and even in the targeted search there are many AGN which are too
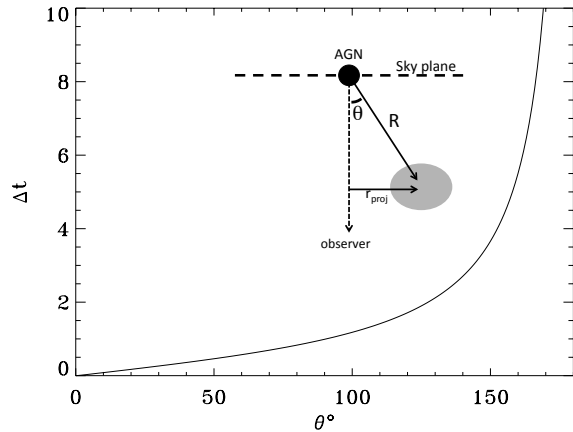
through the highest recombination-line surface brightness in the clouds.

Figure 13. Behavior of the differential time delay Δt between radiation seen directly from the nucleus and reprocessed through a cloud at distance R from the nucleus, as a function of angle θ from the line of sight, for fixed value of projected radius r_{proj}. The inset diagram shows the geometric quantities. Units of Δt are r_{proj}/c.

weak to ionize the extended gas; in essence, given a luminous AGN, our selection is for objects with outlying gas available to be ionized. In a toy model where all objects' delay times Δt are equal, the timescale for the AGN to be at high luminosity before fading would be of order $\Delta t n_{bright}/n_{faded}$. From Table 6, our estimate is $1.2\Delta t$ when we divide the bright and faded groups at an ionizing/FIR ratio of 1.5. The projected extent of the clouds r_{max} from our [O III] data is listed in table 8; for the 19 galaxies in our sample, the mean value is 19 kpc with a median of 17. For a typical projected extent 20 kpc, this becomes a range 25,000–175,000 years, taking the sample to populate values of $\theta = 90 \pm 50°$ at this small sample size. For the luminosity range of Seyfert galaxies we have probed, the fading may be an order of magnitude in ionizing luminosity, but this sample includes no cases in which we see AGN-ionized clouds around a galaxy with no optical trace of an AGN. IC 2497 (Lintott et al. 2009) must be extreme in this respect, having faded from a QSO to a borderline LINER./Sy 2 nucleus. As noted by Schawinski et al. (2010a), these timescales are rapid compared to expectations from scaling up the behavior of accretion disks around stellar-mass black holes, perhaps indicating that disk self-gravity enhances the growth of accretion instabilities.

There are several directions in which we can expand this study. In a "Dead Quasar Survey", we are conducting [O III] imaging of samples of luminous AGN hosts and galaxies without AGN signatures, to seek fainter (and possibly older) clouds than can be detected from the SDSS g images. H I selection should help pick out objects with tidal tails in suitable positions to be ionized at tens of kpc from the core; we are beginning with the Kuo et al. (2008) sample of Seyfert galaxies mapped in H I. For the "faded" galaxies in thes sample, we are pursuing *XMM-Newton* and *HST* observations to clarify the obscuration toward the nucleus, seek any signs of outflow-induced star formation as seen in Hanny's Voorwerp, and refine estimates of the ionizing luminosity

REFERENCES

Alonso, M. S., Lambas, D. G., Tissera, P., & Coldwell, G. 2007, MNRAS 375, 1017

Antonucci, R. 1993, ARA&A 31, 473

Baldwin, J.A., Phillips, M.M. & Terlevich, R. 1981, PASP 93, 5

Barbosa, F.K.B., Storchi-Bergmann, T., Cid Fernandes, R., Winge, C. & Schmitt, H. 2009, MNRAS 396, 2

Bennert, N. 2005, Ph.D. dissertation, Ruhr-Universität Bochum

Bennert, N., Jungwiert, B., Komossa, S., Haas, M. & Chini, R. 2006a, A&A 446, 919

Bennert, N., Jungwiert, B., Komossa, S., Haas, M. & Chini, R. 2006b, A&A 456, 953

Bianchi, S., Chiaberge, M., Piconcelli, E., Guainazzi, M. & Matt, G. 2008, MNRAS 386, 105

Capetti, A., Macchetto, F., Sparks, W. B., & Boksenberg, A. 1994, ApJ 421, 87

Chatzichristou, E.T. & Vanderriest, C. 1995, A&A 298, 343

Condon, J.J. & Broderick, J.J 1988, AJ 96, 30

Condon, J.J., Cotton, W.D., Greisen, E.W., Yin, Q.F., Perley, R.A., Taylor, G.B. & Broderick, J.J. 1998, AJ. 115, 1693

Cracco, V. et al. 2011, MRAS (in the press), arXiv:1109.1195

Dadina, M., Guainazzi, M., Cappi, M., Bianchi, S., Vignali, C., Malaguti, G., & Comastri, A. 2010, A&A 516, A9

da Silva, R.L., Prochaska, J.X., Rosario, D., Tumlinson, J., & Tripp, T.R. 2011, ApJ (in the press) =arXiv 1103.4134v1

Dopita, M.A. & Sutherland, R.S. 1996, ApJS 102, 161

Fesen, R. A., Blair, W. P., & Kirshner, R. P. 1982, ApJ 262, 171

Filippenko, A.V. 1982, PASP 94, 715

Fischer, T. C., Crenshaw, D. M., Kraemer, S. B., Schmitt, H. R., Mushotsky, R. F., & Dunn, J. P. 2011, ApJ 727, 71

Fu, H. & Stockton, A. 2009, ApJ 690, 953

Fu, H. & Stockton, A. 2009, ApJ 696, 693

Fullmer, L. & Lonsdale, C.J. 1989, Cataloged Galaxies and Quasars Observed in the IRAS Survey, Version 2, Jet Propulsion Laboratory (JPL D-1932)

Josza, G.I.G. et al. 2009, A&A 500, l33

Kauffmann, G. et al. 2003, MNRAS, 346, 1055

Kawada, M. et al. 2007, PASJ 59, S389–S400

Keel, W.C. 1983, ApJ 269, 466

Keel, W.C. 1996, ApJS 106, 27

Keel, W.C., et al. 2011, in preparation

Kewley, L. J., Dopita, M. A., Sutherland, R. S., Heisler, C. A., & Trevena, J. 2001, ApJ, 556, 121

Komossa S. & Schulz, H. 1997 A&A 323, 31

Koss, M., Mushotzky, R., Treister, E., Veilleux, S., Vasudevan, R., Miller, N., Sanders, D.B., Schawinski, K., & Trippe, M 2011, ApJL 735, L42

Kuo, C.-Y., Li, J., Tang, Y.-W., & Ho, P.T.P. 2008, ApJ 679, 1047

Li, C., Kauffmann, G., Heckman, T. M., White, S. D. M., & Jing, Y. P. 2008, MNRAS 385, 1915

Lintott, C. J., et al. 2008, MNRAS, 389, 1179

Lintott, C. J., et al. 2009, MNRAS, 399, 129

Lupton, R., Blanton, M. R., Fekete, G., Hogg, D. W., O'Mullane, W., Szalay, A., & Wherry, N. 2004, PASP, 116, 133

Maia, M. A. G., Machado, R. S., & Willmer, C. N. A. 2003, AJ 126, 1750

Mazzarella, J.M., Soifer, B.T., Graham, J.R., Neugebauer, G., Matthews, K. & Gaume, R.A. 1991, AJ 102, 1241

Michitoshi, Y. et al. 2004, AJ 127, 90

Moran, E.C., Halpern, J.P., Bothun, G.D., & Becker, R.H. 1992, AJ 104, 990

Morse, J. A., Winkler, P. F., & Kirshner, R. P. 1995, AJ 109, 2104

Murakami, H., et al., 2007, PASJ 59, S369–S376

Osterbrock, D.E. 1977, ApJ 215, 733

Pedlar, A., Meaburn, J., Axon, D. J., Unger, S. W., Whit-

Table 1. Spectroscopic data

Telescope	UT Dates	Range, Å	Resolution, Å	Slit scale "/pixel	Galaxies observed
KPNO 2.1m	2010 June 15-21	3630-5700	3.2	0.78	33
Lick 3m	2010 July 12-15	5450-8260	4.5	0.78	11
		3495-5605	1.5	0.43	11
Lick 3m	2010 Dec 1 - 3	4630-7410	4.3	0.78	13
		3280-4595	2.7	0.43	13
Lick 3m	2009 Dec 17	5250-9940	13.5	0.78	2
		3650-5710	4.8	0.43	2

tle, D. M., Meurs, E. J. A., Guerrine, N., & Ward, M. J. 1989, MNRAS 238, 863

Prieto, M.A. & Freudling, W, 1996, MRAS 279, 63

Ramos Almeida, C., Pérez García, A. M., Acosta-Pulido, J. A., Rodríguez Espinosa, J. M., Barrena, R., & Manchado, A. 2006, ApJ 645, 148

Rampadarath, H., et al. 2010, A&A 517, 8

Röttgering, H.J.A, Tang, Y., Bremer, M.A.R., de Bruyn, A.G., Miley, G.K. Rengelink, R.B. & Bremer, M.N. 1996, MNRAS 282, 1033

Schawinski, K., et al. 2010a, ApJL 724, L30

Schawinski, K., et al. 2010b, ApJ, 711, 284

Schmitt, H.R., Kinney, A.L., Storchi-Bergmann, T. & Antonucci, R. 1997, ApJ 477, 623

Shaw, R.A. & Dufour, R. J. 1995, PASP 107, 896

Spergel, D. N., et al. 2007, ApJS 170, 377

Stasińska, G., Cid Fernandes, R., Mateus, A., Sodré, L., & Asari, N. V. 2006, MNRAS 371, 972

Stockon, A., Fu, H. & Canalizo, G. 2006, NewAR 50, 694

Tadhunter, C. & Tsvetanov, Z. 1989, Nature 341, 422

Tody, D. 1986, SPIE 627, 733

Unger, S.W., Pedlar, A., Axon, D.J., Whittle, M., Meurs, E.J.A., & Ward, M.J. 1987, MNRAS 228, 671

Uomoto, A., Caganoff, S., Ford, H.C., Rosenblatt, E.I., Antonucci, R.R.J., Evans, I.N., & Cohen R.D. 1993, AJ 1-5, 1308

Veilleux, S. & Osterbrock, D.E. 1987, ApJS 63, 295

Veron-Cetty, M.P. & Veron, P. A&A 518, 10

Wallerstein, G. & Balick, B. 1990, MNRAS 245, 701

Whittle, D.M., Rosario, D., Silverman, J.D., Nelson, C.H. & Wilson, A.S. 2005, AJ 129, 104

Whittle, D.M. & Wilson, A.S. 2004, AJ 127, 606

Wilson, A.S. 1996, VA 40, 63

Wilson, A.S. & Tsvetanov, Z. 1994, AJ 107, 1227

Wu, Y.-Z., Zhang, E.-P., Liang, Y.-C., Zhang, C.-M., & Zhao, Y.-H. 2011, ApJ 730, 121

Yamamura, I., Makiuti, S., Ikeda, N., Fukuda, Y., Oyabu, S., Koga, T., & White, G. J., 2010, http://www.ir.isas.jaxa.jp/AKARI/Observation/PSC/Public/RN/AKARI-FIS_BSC_V1_RN.pdf

Yoshida, M., et al. 2002, ApJ 567, 118

Table 2. Candidate AGN with extended emission-line clouds

Coordinate name	SDSS ObjID	z	Nucleus	Name/note	Search	Posted by
SDSS J005607.66+254804.7	587740589487030353	0.1530	Sy 1	purple haze	S	ElisabethB
SDSS J003507.44+004502.1	587731187281494175	0.1205	LINER	blue arc	S	scott L
SDSS J004527.06+004237.6	587731187282608299	0.1096	Sy 1.5		S	davidjamesjones
SDSS J013037.75+131251.9	587724197207212176	0.0721	Sy 2	CGCG436-065	T	
SDSS J014238.47+000514.7	588015509280587804	0.1459	Sy 1		S	Tsering
SDSS J014644.82-004043.1	588015508207304746	0.0827	Sy 1		S	davidjamesjones
SDSS J030526.96+005144.9	588015510363373793	0.1181	Sy 1		S	Mukund Vedapudi
SDSS J030639.58+000343.2	588015509289762862	0.1074	Sy 1		S	Mitch
SDSS J033013.26-053235.9	587724242842026028	0.0131	Sy 1	NGC 1346	S	Half65
SDSS J040548.78-061925.7	587727178476093634	0.0556	Sy 1		S	echo-lily-mal
SDSS J074241.70+651037.8	758878270293868614	0.0371	Sy 2	Mkn 78	T	
SDSS J075910.44+115156.7	588023046395527377	0.0503	Sy 1		S	silverhaze
SDSS J080452.73+212050.2	588016878287650850	0.1242	Sy 1	purple haze	S	davidjamesjones
SDSS J082034.78+153111.3	587741532229337219	0.1435	Sy 1		S	Half65
SDSS J082342.37+482754.4	587725470667833620	0.0935	Sy 2		S	spiralmania
SDSS J082642.63+111555.5	587745244691628370	0.0884	trans		T	
SDSS J083525.51+104925.7	587744873714679862	0.1172	Sy 1		S	spiralmania
SDSS J083818.43+333441.3	587732470387703859	0.0621	LINER	KUG	T	
SDSS J084002.36+294902.6	587735240637284507	0.0648	Sy 2	4C 29.30	T	
SDSS J084344.98+354942.0	587732484342415393	0.0539	Sy 2		S T	laihro
SDSS J084518.51+142034.1	587742062124269645	0.0606	Sy 1	purple haze	S	mitch
SDSS J084810.10+351534.0	587732470388818038	0.0573	Sy 2	KUG0845+354	T	
SDSS J084809.59+351530.3	587732470388818042	0.0567	Sy 2	KUG0845+354	T	
SDSS J084917.31+531755.7	587725470670585957	0.1112	Sy 1	purple haze	S	Tsering
SDSS J085625.93+021310.5	587727944563884115	0.1251	RG		S	Bruno
SDSS J085729.84+064210.6	587734691423453446	—	—		S	lovethetropics
SDSS J085837.52+182221.5	587741708866289722	0.0588	Sy 2		T	
SDSS J085813.75+385631.8	587732053243855000	0.0884	Sy 2		T	
SDSS J090547.33+374738.2	587732152565432366	0.0475	trans		T	
SDSS J090958.07+621450.4	587737826756198431	0.0261	Sy 2	NGC 2742A	S	Ioannab
SDSS J091011.34+230717.9	587741421104136355	0.0362	—		S	Citizen_Kirk
SDSS J091708.26+292215.6	587738946130018402	0.0353	Sy 2	KUG 0914+295	S	Half65
SDSS J093033.05+034443.6	587728880335257753	0.0911	Sy 1		S	ElisabethB
SDSS J094529.64-002154.7	587725074458345485	0.0515	LINER		T	
SDSS J095559.88+395446.9	588016528244670522	0.0483	—	violet plume	S	StephanieC
SDSS J100507.88+283038.6	587741392112451744	0.0517	Sy 2		S T	stellar190
SDSS J100529.60+275844.2	587741391575580675	0.0555	Sy 2		S	mitch
SDSS J101128.26+260655.4	587741490365792357	0.1164	Sy 2		S	mitch
SDSS J101645.11+421025.5	588297863112294442	0.0553	NLSy1		S	mitch
SDSS J102016.20+524756.9	587731499185602761	0.0689	Sy 2		S	
SDSS J102108.59+024058.5	587726033311498259	—			S	mitch
SDSS J103734.22+140120.5	587735349101199404	0.2061	Sy 2		S	davidjamesjones
SDSS J104232.05+050241.9	587728880879992930	0.0271	Sy 2	NGC 3341	S	mitch
SDSS J104326.47+110524.2	587734948595499096	0.0475	Sy 1	purple haze	S	lovethetropics
SDSS J104515.28+421331.7	588017626147782828	0.0990	LINER	bubble?	S	RandyC
SDSS J110157.90+101739.2	587732772658806856	0.0340	Sy 1		S	davidjamesjones
SDSS J110335.42+032014.7	587726033853022296	0.0531	Sy 2		S	skwalker
SDSS J110445.46+041755.2	588010358543351857	0.0252	Sy 2		S	ElisabethB
SDSS J110756.53+474434.8	588295840708755475	0.0727	Sy 1		S	davidjamesjones
SDSS J111100.60-005334.9	588848898833580220	0.0904	Sy 2		S T	ElisabethB
SDSS J111113.00+284242.7	587741532784361479	0.0294	SB	NGC 3561A	T	
SDSS J111113.18+284147.0	587741532784361477	0.0295	Sy 2	NGC 3561	T	
SDSS J111349.74+093510.7	587734892748144649	0.0292	Sy 1.5	IC 2637	S T	stellar190
SDSS J111653.96+593146.8	587729387686461462	0.0815	trans	VII Zw 384	T	
SDSS J112534.58+523247.0	587732136456487055	0.0270	SB		S	errattan
SDSS J112753.87+302138.6	587741491447070913	0.0736	nonAGN		S	paulrogers
SDSS J112942.51+235014.1	587742189363331247	0.1277	LINER		S	ElisabethB
SDSS J113323.97+550415.8	587733081347063838	0.0085	Sy 1	Mkn 177 compn	S	stellar190
SDSS J113629.36+213551.7	587742013279502427	0.0297	Sy 1	Mkn 739	S T	Budgieye
SDSS J113849.61+574243.4	587735696978215000	0.1162	Sy 1		S	ElisabethB
SDSS J114155.61+010516.7	588848901521277093	0.1365	Sy 2		S	lovethetropics

Table 2 – *continued*

Table 3 – *continued* Candidate AGN with extended emission-line clouds

Coordinate name	SDSS ObjID	z	Nucleus	Name/note	Search	Posted by
SDSS J114454.85+194635.3	588023669168537695	0.0274	Sy 2		S T	stellar190
SDSS J114517.10+200121.8	588023669705474229	0.04953	—	(possible)	S	Half65
SDSS J115140.70+675041.9	587725552285122567	0.0629	Sy 2		S	StephanieC
SDSS J115739.07-023908.3	587724649256779921	0.1308	Sy 1	purple haze	S	c_cld
SDSS J115906.89+101001.7	587732771591225359	0.1165	Sy 1.8	purple haze	S	c_cld
SDSS J120114.35-034041.0	587725039018311737	0.0196	Sy 1	Mkn 1310	S	Milk_n_cookies
SDSS J120150.80+143323.9	587735348036370587	0.0677	nonAGN		S	DuffBeer
SDSS J120719.81+241155.8	587742189367066665	0.0505	NLSy1	purple haze Mkn 648	S	davidjamesjones
SDSS J120939.43+643107.6	587729154134966352	0.1042	Sy 2		S	mitch
SDSS J121418.25+293146.7	587741532253519916	0.0632	Sy 2	Was 49ab	S T	stellar190
SDSS J121431.32+402902.6	588017979429486656	0.1211	Sy 2		S	mitch
SDSS J121452.41+591953.2	587729386079059975	0.0607	Sy 2	VII Zw 444	S	mitch
SDSS J121553.08+051447.8	588010359624827047	0.0803	LINER		S	codexluminati
SDSS J121819.30+291513.0	587739719750058064	0.0477	Sy 2	UGC 7342	S T	stellar190
SDSS J122402.57+435814.0	588017603610935505	0.1040	nonAGN		S	fluffyporcupine
SDSS J122546.72+123942.7	588017566564155399	0.0086	Sy 2	NGC 4388	S T	RandyC
SDSS J122802.10+094347.9	587733771057434918	0.1534	LINER		S	Bruno
SDSS J123034.25+033800.7	587726016682917948	0.01285	LINER		S	StephanieC
SDSS J123038.98+401614.4	587738947758456849	0.1322	Sy 1.5	purple haze	S	Tsering
SDSS J123046.11+103317.3	587732772131504164	0.01540*	SB*	VPC 0764	S	lovethetropics
SDSS J123113.12+120307.2	588017702933823557	0.1161	Sy 1		S	lovethetropics
SDSS J124036.73+365004.3	587739096991334439	0.0404	Sy 2		S	stellar190
SDSS J124046.40+273353.5	587741602034090027	0.0565	Sy 1.5		S	Tsering
SDSS J124103.66+273526.0	587741602034155555	0.2007	Sy 1		S	Tsering
SDSS J124325.65+365525.3	587739096991596570	0.0839	Sy 2		S	Bruno
SDSS J124450.84-042604.5	587745544806727722	0.0147*	LINER*	IC 0812	S	Milk_n_Cookies
SDSS J124505.56+102433.2	587732772133011652	0.0976	Sy 2		S	davidjamesjones
SDSS J124511.84+230210.0	587742014897127434	0.02326	—	IC 0813	S	Elizabeth
SDSS J125741.04+202347.7	588023670249750583	0.0807	Sy 2	IC 3929	S T	c_cld
SDSS J130007.06+183914.3	587742575372730410	0.1130	Sy 2		S	mitch
SDSS J130234.89+184122.3	588023668102856809	0.0656	Sy 2		S	Mukund Vedapudi
SDSS J130422.19+361543.1	587738950954385445	0.0443	Sy 2	WR 470	S	mitch
SDSS J130258.82+162427.7	587742773491531836	0.0673	Sy 1	Mkn 783	S	stellar190
SDSS J130509.98-033209.2	587725039025258588	0.0835	Sy 1	purple haze	S	lovethetropics
SDSS J131555.15+212521.5	587742013289660465	0.0884	Sy 1		S T	davidjamesjones
SDSS J131639.74+445235.0	588017605762482225	0.0909	Sy 1.9		S	c_cld
SDSS J131913.93+132030.8	587736802936684556	0.0960	Sy 2		S	mitch
SDSS J132340.31-012749.1	587725041711644785	0.0767	Sy 1	IC 1101	S	
SDSS J132540.23+275146.1	587739719219675227	0.0377			S	ElisabethB
SDSS J133227.20+112910.4	588017570316615795	0.0778	Sy 2		S	veggy2
SDSS J133416.49+311709.1	587739609171230755	0.0570	SB	Was 75	T	
SDSS J133718.72+242303.3	587742190986657795	0.1076	NLSy1		S	c_cld
SDSS J133815.86+043233.3	587729158970736727	0.0228	Sy 1.5	NGC 5252	S T	laihro
SDSS J133817.11+481636.1	587732483292266549	0.02786	Sy 2	NGC 5256, Mkn 266	S T	ElisabethB
SDSS J134442.16+555313.5	587735666377949228	0.0373	Sy 2	Mkn 273	S T	stellar190
SDSS J134608.10+293810.4	587739504478060626	0.0776	Sy 1		S	lovethetropics
SDSS J134630.29+283646.3	587739707943092392	0.0518	Sy 2		T	
SDSS J135255.67+252859.6	587739810484650051	0.06387	Sy 1	KUG1350+257	T	
SDSS J135602.62+182217.7	587742550676275314	0.0506	Sy 2	Mkn 463	T	
SDSS J135635.73+232135.9	587739845379883044	0.0668	LINER		T	
SDSS J135712.06-070433.0	5877462362982311865	—			S	stellar190
SDSS J140037.11+622132.7	587728918446407773	0.0752	Sy 1		S	mitch
SDSS J141051.82+410412.5	588017604156457121	0.0812	LINER		S	Song
SDSS J140506.26+024618.2	587726033335943373	0.0766	Sy 2		S	mitch
SDSS J141405.01+263336.8	587739720298201117	0.0357	Sy 1		S	davidamesjones
SDSS J142522.28+141126.5	587742609727684701	0.0601	Sy 2		T	
SDSS J142925.07+451831.8	587735490282848380	0.0748	Sy 1.5	purple haze	S T	Aroel
SDSS J143029.88+133912.0	587736809916399664	0.0852	Sy 2	Teacup	S T	Half65
SDSS J143239.83+361808.0	587736583892238376	0.0132	Sy 2/SB	NGC 5675	T	
SDSS J144038.10+533015.8	587733427086426161	0.0376	Sy 2	Mkn 477	T	

Table 2 – *continued*

Table 3 – *continued* Candidate AGN with extended emission-line clouds

Coordinate name	SDSS ObjID	z	Nucleus	Name/note	Search	Posted by
SDSS J144240.79+262332.5	587739457225097282	0.1071	Sy 1		S	spiralmania
SDSS J144331.19+191121.0	587742062161428638	0.0598	Sy 2		S	Bruno
SDSS J145724.63+105937.3	587736807771930760	0.1227	Sy 1		S	davidjamesjones
SDSS J150756.88+032037.3	587726100952449048	0.1369	Sy 1		S	mitch
SDSS J151004.01+074037.1	588017991773520114	0.0458	Sy 2		S T	Blackprojects
SDSS J150408.46+143123.3	587742575922708553	0.1181	Sy 1	Mkn 840	S	mitch
SDSS J151141.26+051809.2	587736546312323142	0.0845	Sy 1		S	Half65
SDSS J151915.98+104847.8	587736813131989104	0.0988	Sy 1		S T	spiralmania
SDSS J152412.58+083241.2	588017703489372418	0.0371	Sy 2		S T	spiralmania
SDSS J152549.54+052248.7	587730022796755031	0.048	Sy 2		T	
SDSS J152907.45+561606.6	587742882456731737	0.0998	Sy 1		S	spiralmania
SDSS J153355.15+585756.4	587725818571063416	—			S	lovethetropics
SDSS J153432.52+151133.2	587742013841145937	0.0066	Sy 2	NGC 5953	S	Half65
SDSS J153508.93+221452.8	587739814240190581	0.0858	trans	purple haze	T	
SDSS J153703.36+135944.1	587742590401904799	0.0737	LINER		S	RandyC
SDSS J153854.16+170134.2	587739845390761994	0.02974	Sy 2	NGC 5972	S T	NeilGibson
SDSS J155007.62+272814.5	587736941990969374	0.1468	Sy 1	purple haze	S	ElisabethB
SDSS J160536.79+174807.5	587739720846934175	0.0339	Sy 2	IC 1182	S	stelar190
SDSS J162538.08+162718.1	587739814246023211	0.0343	LINER	Akn 502	T	
SDSS J162804.06+514631.4	587736980102643827	0.0547	Sy 1.9	Mkn 1498	S	Budgieye
SDSS J162930.01+420703.2	587729653421441105	0.0717	Sy 1	purple haze	S	Tsering
SDSS J162952.88+242638.4	587736898503639075	0.0368	Sy 1	Mkn 883	S T	ElisabethB
SDSS J164800.81+295657.4	587733399186898947	0.1059	Sy 1		S	mitch
SDSS J172335.75+342133.4	587739849686843709	—			S	Mukund Vedapudi
SDSS J172747.17+265121.4	587729409160183880	0.0291		VV 389	S	elizabeth
SDSS J172935.81+542939.9	587725505559855518	0.0820	Sy 2		S	Bruno
SDSS J181611.61+423937.3	758879745074397535	0.04120	Sy 2	UGC 11185	S	stellar190
SDSS J210918.38-060754.7	587726879412256901	0.0286	Sy 2		S	mitch
SDSS J214150.10+002209.4	587731186725683280	0.1068	LINER		S	echo-lily-mal
SDSS J220141.64+115124.3	587727221400862869	0.0296	Sy 2		S T	stellar190
SDSS J233254.46+151305.4	587730774959652922	0.2148	Sy 1		S	ElisabethB
SDSS J234413.61+004813.9	587731187275923676	0.0497	LINER		S	davidjamesjones

Table 4. Results of long-slit spectroscopy

Coordinate name	SDSS ObjID	z	Nucleus	Name	PA°	Source	Region Type
Confirmed AGN-ionized:							
SDSS J074241.70+651037.8	758878270293868614	0.0371	Sy 2	Mkn 78	90	Lick	AGN
SDSS J095559.88+395446.9	588016528244670522	0.0483*	Sy 2*		148	Lick	AGN
SDSS J100507.88+283038.5	587741392112451744	0.0517	Sy 2		62	Lick	AGN
SDSS J111349.74+093510.7	587734892748144649	0.0292	Sy 1.5	IC 2637	47	GCam	AGN
SDSS J113629.36+213551.7	587742013279502427	0.0297	Sy 1	Mkn 739	168	GCam	AGN
SDSS J121819.30+291513.0	587739719750058064	0.0477	Sy 2	UGC 7342	133	GCam	AGN
SDSS J122546.72+123942.7	588017566564155399	0.0086	Sy 2	NGC 4388	26	GCam	AGN
SDSS J133815.86+043233.3	587729158970736727	0.0228	Sy 1.5	NGC 5252	175	GCam	AGN
SDSS J133817.11+481636.1	587732483292266549	0.0279	Sy 2	Mkn 266	176	GCam Lick	AGN
SDSS J134442.16+555313.5	587735666377949228	0.0373	Sy 2	Mkn 273	57	GCam	AGN
SDSS J135602.62+182217.8	587742550676275314	0.0504	Sy 2	Mkn 463	8	GCam	AGN
SDSS J143029.88+133912.0	587736809916399664	0.0852	Sy 2	Teacup	37	GCam Lick	AGN
SDSS J151004.01+074037.1	588017991773520114	0.0458	Sy 2		175	GCam	AGN
SDSS J152412.58+083241.2	588017703489372418	0.0371	Sy 2	CGCG 077-117	150	GCam	AGN
SDSS J153854.16+170134.2	587739845390761994	0.0297	Sy 2	NGC 5972	167	GCam Lick	AGN
SDSS J162804.06+514631.4	587736980102643827	0.0547	Sy 1.9	Mkn 1498	150	GCam Lick	AGN
SDSS J162952.88+242638.4	587736898503639075	0.0368	Sy 1	Mkn 883	91	Lick	AGN
SDSS J181611.61+423937.3	758879745074397535	0.0412	Sy 2	UGC 11185	90	GCam Lick	AGN
SDSS J220141.64+115124.3	587727221400862869	0.0296	Sy 2		19	GCam Lick	AGN
Other cloud types:							
SDSS J003507.44+004502.1	587731187281494175	0.1205	LINER		35	Lick	H II regions
SDSS J005607.66+254804.7	587740589487030353	0.1530	Sy 1		200	Lick	no
SDSS J012839.87+144553.8	587724233179660360	0.0452	Sy 2	CGCG436-060	45	Lick	no
SDSS J014238.47+000514.7	588015509280587804	0.1459	Sy 1		80	Lick	AGN
SDSS J030639.58+000343.2	588015509289762862	0.1074	Sy 1		40	Lick	AGN (small)
SDSS J033013.26-053235.9	587724242842026028	0.0131	SB*	NGC 1346	76	Lick	H II
SDSS J040548.78-061925.7	587727178476093634	0.0556	Sy 1		76	Lick	H II
SDSS J080452.73+212050.2	588016878287650850	0.1242	Sy 1		150	Lick	AGN (small)
SDSS J082642.63+111555.5	587745244691628370	0.0884	trans		72	Lick	resolved?
SDSS J083525.51+104925.7	587744873714679862	0.1172	Sy 1		150	Lick	small?
SDSS J084344.98+354942.0	587732484342415393	0.0539	Sy 2		141	Lick	AGN
SDSS J111100.60-005334.9	588848898833580220	0.0904	Sy 2		101	GCam	unresolved cloud at 4"
SDSS J113323.97+550415.8	587733081347063838	0.0085	Sy 1	Mkn 177	136	GCam	AGN in small compn
SDSS J114454.85+194635.3	588023669168537695	0.0274	Sy 2		131	GCam	unresolved < 2"
SDSS J121418.25+293146.7	587741532253519916	0.0632	Sy 2	Was 49ab	63	GCam	off-nuc AGN or cloud
SDSS J123046.11+103317.3	587732772131504164	0.01540	SB	VPC 0764	30	GCam	unresolved
SDSS J124450.84-042604.5	587745544806727722	0.0147*	LINER*	IC 0812	62	GCam	< 2"
SDSS J125741.04+202347.7	588023670249750583	0.0807	Sy 2	IC 3929	47	GCam	H II to 9"
SDSS J134630.29+283646.3	587739707943092392	0.0518	Sy 2		164	GCam	34" dim AGN cloud?
SDSS J135255.67+252859.6	587739810484650051	0.06387	Sy 1	KUG1350+257	163	GCam	H II
SDSS J142522.28+141126.5	587742609727684701	0.0601	Sy 2		110	GCam	two AGN?
SDSS J150408.46+143123.3	587742575922708553	0.1181	Sy 1	Mkn 840	70	GCam	7"
SDSS J151915.98+104847.8	587736813131989104	0.0099	Sy 1		89	GCam	unresolved < 2"
SDSS J153508.93+221452.8	587739814240190581	0.0858	trans		70	GCam	< 2"
SDSS J153703.36+135944.1	587742590401904799	0.0737	LINER		21	GCam	unresolved
SDSS J160536.79+174807.5	587739720846934175	0.0339	Sy 2	IC 1182	96	GCam	H II
SDSS J210918.38-060754.7	587726879412256901	0.0286	Sy 2		70	GCam	unresolved < 2"
SDSS J214150.10+002209.4	587731186725683280	0.1068	LINER		70	GCam Lick	unresolved < 2"
SDSS J233254.46+151305.4	587730774959652922	0.2148	Sy 1		138	Lick	unresolved < 2"
SDSS J234413.61+004813.9	587731187275923676	0.0497	LINER		71	Lick	H II

Table 5. Emission-line ratios and selected fluxes

Object		$\frac{[\text{Ne V}]\lambda3426}{[\text{Ne III}]\lambda3869}$	$\frac{[\text{Ne III}]\lambda3869}{[\text{O II}]\lambda3727}$	$\frac{[\text{O II}]\lambda3727}{[\text{O III}]\lambda5007}$	$\frac{\text{He II}\lambda4686}{\text{H}\beta}$	$\frac{[\text{O III}]\lambda5007}{\text{H}\beta}$	F(5007)	$\frac{[\text{OI}]\lambda6300}{\text{H}\alpha}$	$\frac{[\text{NII}]\lambda6583}{\text{H}\alpha}$	$\frac{[\text{SII}]}{\text{H}\alpha}$	F(Hα)
IC 2637	nuc	0.23	0.28	0.81	0.11	3.94	2.7e-14				
	cloud	< 0.2	0.12	2.43	< 0.06	1.34	4.6e-15				
Mkn 78	nuc (1)	0.35	0.32	0.10	0.29	13.5	6.8e-14	0.05	1.00	0.23	6.5e-13
	cloud	2.00	0.16	0.43	0.37	14.00	7.8e-15	0.094	0.51	0.22	2.0e-15
Mkn 266	nuc	0.69	0.17	0.43	0.19	4.08	3.4e-14	0.052	0.58	0.35	4.0e-14
	cloud	0.46	0.40	0.22	0.38	8.20	3.7e-14	0.029	0.25	0.23	1.1e-14
Mkn 273	nuc	0.27	0.11	0.90	0.12	3.93	2.4e-14				
	cloud	0.06	0.26	0.93	0.27	9.3	1.0e-14				
Mkn 463	nuc	0.26	0.29	0.30	0.08	7.7	3.7e-13				
	cloud	0.41	0.16	0.51	0.17	11.3	1.8e-14				
Mkn 739	nuc (2)	1.16	0.49	0.15	0.18	5.88	1.5e-14				
	cloud	1.31	0.22	0.45	0.24	8.30	6.5e-15				
Mkn 883	nuc	0.31	0.12	0.81	0.08	2.82	5.3e-14	0.12	0.47	0.47	8.4e-13
	cloud	0.30	0.22	0.30	0.19	7.84	6.6e-15	0.08	0.31	0.49	4.1e-15
Mkn 1498	nuc (2)	0.73	0.82	0.07	0.10	3.72	1.5e-13	0.07	1.00	0.22	4.9e-14
	cloud	1.08	0.62	0.18	0.32	12.3	1.0e-14	0.06	0.14	0.20	3.4e-15
NGC 4388	nuc	0.45	0.25	0.27	0.23	11.5	3.6e-13				
	cloud	0.39	1.15	0.57	< 0.23	4.72	4.3e-15				
NGC 5252	nuc	0.31	0.27	0.55	0.19	9.22	6.0e-14				
	cloud	1.31	0.34	0.31	0.34	10.1	1.1e-14				
NGC 5972	nuc	2.25	0.31	0.29	0.40	2.56	5.1e-14	0.07	0.69	0.49	1.9e-14
	cloud	0.15	0.20	0.63	0.26	8.48	2.6e-14	0.12	0.79	0.61	9.5e-15
SDSS 0955+39	nuc	< 0.54	0.05	4.60	< 0.04	2.90	6.9e-16	0.32	0.84	1.02	1.6e-15
	cloud	2.64	0.47	0.28	0.51	7.00	3.2e-15	0.08	0.26	0.37	9.5e-16
SDSS1005+28	nuc	0.55	0.29	0.30	0.24	7.96	1.1e-14	0.07	0.57	0.48	5.8e-15
	cloud	1.52	0.60	0.24	0.58	5.46	4.5e-15	< 0.01	0.25	0.34	3.3e-15
SDSS 1510+07	nuc	0.04	1.15	1.86	< 0.01	2.11	3.2e-15				
	cloud	1.76	0.22	0.56	0.39	6.64	4.4e-15				
SDSS 1524+08	nuc	0.78	0.19	0.91	0.37	8.00	4.8e-15				
	cloud	1.58	0.15	0.49	0.44	7.84	5.4e-15				
SDSS 2201+11	nuc	0.17	0.07	1.65	0.28	5.48	1.7e-15	0.17	1.21	1.02	7.0e-15
	cloud	0.53	0.24	0.21	0.18	10.1	7.8e-15	0.07	0.40	0.35	3.0e-15
Teacup	nuc	0.31	0.23	0.30	0.09	7.95	1.3e-13	0.15	0.23	0.15	1.1e-14
	cloud	0.14	0.17	0.23	0.15	8.07	2.1e-14	0.11	0.34	0.36	7.6e-15
UGC 7342	nuc	0.75	0.22	0.58	0.22	9.14	2.9e-14				
	cloud	0.77	0.26	0.41	0.55	9.90	8.9e-15				
UGC 11185	nuc (1)	0.17	0.19	0.37	0.16	8.89	8.5e-14	0.19	1.29	0.88	3.8e-14
	cloud	0.28	0.28	0.25	0.26	8.11	1.4e-14	0.07	1.10	0.72	5.1e-15

Notes: Line fluxes are in units of erg cm^{-2} s^{-1}
(1) blend of two velocity components
(2) BLR present; flux is estimated NLR only

Table 6. Ionizing and far-infrared luminosity comparison

SDSS ID	Other name	IRAS 60μ	100μ	Akari 90μ	140μ	L(FIR)	r''	F(Hβ)	α°	L_{ion}	Ratio
074241.70+651037.8	Mkn 78	1.11	1.13	0.9 ± 0.2	1.4 ± 0.1	2.4e44	10	4.0e-16	11	> 5.7e43	0.25
095559.88+395446.9		–	–	1.2 ± 0.2	2.5 ± 0.3	5.0e44	7	2.5e-16	16	> 3.0e43	0.06
100507.88+283038.5		–	–	–	–	< 2.1e44	8	4.2e-16	14	> 1.0e44	0.5
111349.74+093510.7	IC 2637	1.75	3.39	2.6 ± 0.1	4.0 ± 0.7	3.0e44	10	3.0e-16	11	> 2.7e43	0.10
113629.36+213551.7	Mkn 739	1.3	2.4	1.7 ± 0.07	3.5 ± 0.6	2.3e44	18	2.1e-16	6.3	> 6.1e43	0.26
121819.30+291513.0	UGC 7342	< 0.2	< 0.6	–	–	< 1.1e44	35	1.8e-16	43.2	> 4.4e44	3.6
122546.72+123942.7	NGC 4388	10.0	17.1	10.4 ± 0.6	15 ± 3	1.4e44	15	3.8e-16	7.6	> 6.3e42	0.02
133815.86+043233.3	NGC 5252	< 0.2	< 0.6	0.4 ± 0.1	–	4.0e43	32	3.8e-16	3.5	> 2.0e44	5
133817.11+481636.1	Mkn 266	7.3	10.3	7.1 ± 0.3	9.0 ± 1.2	1.0e45	27	6.8e-16	4.2	> 3.9e44	0.4
134442.16+555313.5	Mkn 273	22.5	22.5	20.2 ± 0.6	14.3 ± 1.1	5.0e45	12	9.0e-16	10	> 1.6e44	0.03
135602.62+182217.8	Mkn 463	2.33	1.94	1.58 ± 0.03	2.2 ± 0.5	9.0e44	16	3.8e-16	7	> 2.5e44	0.3
143029.88+133912.0	Teacup	0.26	< 0.6	–	–	< 2.3e43	5	1.66e-15	22	> 3.2e44	14
151004.01+074037.1		< 0.2	< 0.6	–	–	< 4e44	14	8.2e-16	8	> 1.3e45	3.4
152412.58+083241.2		0.71	0.73	0.63	< 0.96	1.6e44	5.6e-16	12	10	1.0e44	0.6
153854.16+170134.2	NGC 5972	0.24	< 0.76	–	–	< 5.5e43	35	7.2e-17	3	> 7.8e43	1.8
162804.06+514631.4	Mkn 1498	0.34	< 0.61	–	–	$< 5.$e43	10	9.8e-17	11	> 3.1e43	0.6
162952.88+242638.4	Mkn 883	1.01	1.13	0.84 ± 0.04	–	2.2e44	10	4.0e-16	11	> 5.9e43	0.26
181611.61+423937.3	UGC 11185	< 0.4	< 0.8	–	–	< 1.8e44	10	1.7e-15	11	> 3.1e44	1.7
220141.64+115124.3		0.28	< 0.99	–	–	< 6.1e43	23	4.6e-16	5.0	> 2.0e44	3.4

Notes: FIR fluxes are in Jy
Mean IRAS detection limits are used when no specific value is available
Luminosities are in erg s^{-1}; Hβ fluxes are in erg cm^2 s^{-1}
Values of ionizing/FIR luminosity ratio are all lower limits

Table 7. [S II] density measures and limits

Object	Distance: arcsec	kpc	[S II] ratio	n_e (cm^{-3})	[O II]/[O III]	log U	L_{ion} (erg/s)
Teacup	5-14	8-22	1.25 ± 0.04	130-240	0.15	-2.16	< 1.9e46
Mkn 883	12-16	9-12	1.36 ± 0.03	12- 100	2.62	-3.34	< 4.8e44
SDSS 2201	8-16	5-10	1.48 ± 0.06	< 10	0.25	-2.42	< 2.2e44
NGC 5972	26-30	15-18	1.29 ± 0.12	3-300	0.11	-1.99	< 9.8e46
Mkn 266	20-29	11-16	1.36 ± 0.04	12-100	0.22	-2.36	< 9.3e45

Table 8. Morphologies of AGN hosts with extended clouds

SDSS designation	z	Sy type	Name	r_{max}, kpc	Morphology	cone angle$^\circ$	disc/cloud angle$^\circ$	Sides
SDSS J074241.70+651037.8	0.0371	2	Mkn 78	16	E	55		2
SDSS J095559.88+395446.9	0.0483	2		10	Interacting S	88		1
SDSS J100507.88+283038.5	0.0517	2		13	Sb, disturbed companion	92		1
SDSS J111349.74+093510.7	0.0292	1.5	IC 2637	11	Merger remnant	60		1
SDSS J113629.36+213551.7	0.0297	1	Mkn 739	17	Ongoing merger	28		1
SDSS J121819.30+291513.0	0.0477	2	UGC 7342	38	Ongoing merger; tails	86		2
SDSS J122546.72+123942.7	0.0086	2	NGC 4388	13	Edge-on Sc	80	53	1
SDSS J133815.86+043233.3	0.0228	1.5	NGC 5252	21	Edge-on S0, tilted H I ring	59	31	2
SDSS J133817.11+481636.1	0.0279	2	Mkn 266	21	Ongoing merger	112		2
SDSS J134442.16+555313.5	0.0373	2	Mkn 273	19	Ongoing merger	75		2
SDSS J135602.62+182217.8	0.0504	2	Mkn 463E	16	Ongoing merger	55		2
SDSS J143029.88+133912.0	0.0852	2	Teacup	18	Stellar tail and arc	80		1
SDSS J151004.01+074037.1	0.0904	2		10	Symmetric disc; S0 or Sa	85		2
SDSS J152412.58+083241.2	0.0371	2	CGCG 077-117	19	Merger remnant	56		1
SDSS J153854.16+170134.2	0.0297	2	NGC 5972	33	Warped disc and tails	35	18	2
SDSS J162804.06+514631.4	0.0547	1.9	Mkn 1498	21	E	42		1
SDSS J162952.88+242638.4	0.0368	1	Mkn 883	37	Ongoing merger	73		1
SDSS J181611.61+423937.3	0.0412	2	UGC 11185	11	Strong interaction	48		1
SDSS J220141.64+115124.3	0.0296	2		16	Edge-on warped disc, tails	23	30	2
SDSS J094104.11+344358.4	0.0499	LINER	IC 2497	40	Warped disk, H I tail	46	65	1